INTERNATIONAL JOURNAL FOR NUMERICAL METHODS IN ENGINEERING
Int. J. Numer. Meth. Engng 2007; **69**:1717–1754
Published online 31 July 2006 in Wiley InterScience (www.interscience.wiley.com). DOI: 10.1002/nme.1834

Morphology based domain partitioning of multi-phase materials: A preprocessor for multi-scale modelling

D. M. Valiveti and Somnath Ghosh*, †

Department of Mechanical Engineering, The Ohio State University, 650 Ackerman Road, Columbus, OH 43202, U.S.A.

SUMMARY

This paper develops a microstructural morphology-based domain partitioning method (MDP) as a comprehensive pre-processor for multi-scale simulation of heterogeneous multi-phase materials. The MDP method systematically creates a multi-scale image simulation–characterization methodology to enable domain partitioning that can delineate homogenizable regions from those where explicit representation of phases is necessary for analysis. The methods are strictly based on geometric features of the material morphology and do not use any mechanical response functions. The first step in this development simulates high-resolution microstructural information from low resolution images of the domain and only a limited high resolution micrographs from optical or scanning electron microscopy. The second step uses quantitative characterization of these high resolution images with, e.g. phase distribution functions, to create effective metrics that can relate microstructural features to the material's physical behaviour. The third step invokes domain partitioning to demarcate regions corresponding to different length scales in a concurrent multi-scale model. Partitioning criteria are defined in terms of descriptors of microstructural characteristics and these are used to adaptively create multi-level domain partitions. The method developed is tested on a micrograph of a cast aluminium alloy A356. Copyright © 2006 John Wiley & Sons, Ltd.

Received 6 March 2006; Revised 5 June 2006; Accepted 12 June 2006

KEY WORDS: domain partitioning; microstructure simulation; multiscale characterization

1. INTRODUCTION

Heterogeneous materials like alloy systems, particle reinforced metal matrix composites or fibre reinforced polymer matrix composites are increasingly in use in the automotive, aerospace and other industries. A number of these materials exhibit strong non-uniformities in the micro- and meso-scale composition in the form of morphological variations of, e.g. spatial distributions with

*Correspondence to: Somnath Ghosh, Suite 255, 650 Ackerman Road, The Ohio State University, Columbus, OH, 43202, U.S.A.
†E-mail: ghosh.5@osu.edu

Contract/grant sponsor: National Science Foundation; contract/grant number: CMS-0308666
Contract/grant sponsor: Ohio Supercomputer Center; contract/grant number: PAS813-2

regions of homogeneity, clustering, directionality or connectivity, variations in reinforcement shape and size, or in variations of constituent material and interface properties. Processing methods like powder metallurgy or casting, contribute to these non-uniformities. In multi-phase materials, morphological variations strongly affect the microstructural damage process by phase cracking, interfacial decohesion and matrix rupture by void growth and coalescence, culminating in crack propagation. Failure properties like strain to failure, ductility and toughness are highly sensitive to these variations. For instance, experimental studies with cast aluminium alloy containing silicon and intermetallics inclusions in References [1, 2] have shown that the tensile and fracture behaviour is affected by its microstructure, specifically the shape of inclusions and their spatial distribution. Particles in regions of clustering or specific alignment with respect to loading directions may have a greater propensity towards fracture, than those in regions of dilute concentration due to the fact that local stresses increase rapidly with shorter near neighbour distances [3].

Numerical models of representative volume elements of heterogeneous materials have been developed with high-resolution finite element models to generate overall material response and stress–strain evolution, e.g. in References [4, 5]. A few efforts like Reference [6] have considered limited extensions of the unit cell models with creative boundary conditions to accommodate non-uniform effects. While the predictive capability of these models for the overall response has been satisfactory, their prediction of failure properties like strain-to-failure and fracture toughness is rather limited. These models do not represent the actual local morphology and especially the extreme values of local features, which are critical for failure prediction. Also reasonably large microstructural domains need to be represented in these models. Recently some efforts have been made to model microstructural regions with larger number of spherical heterogeneities in three dimensions [7, 8]. A few studies are also being focused on combining digital image processing and microstructure modelling for more realistic representation of microstructures with non-uniform dispersion of heterogeneities [9–13]. The microstructure based Voronoi cell finite element model (VCFEM) [12–14] offers significant promise in this regard, for analysing large microstructural regions accurately with high efficiency.

The concept of multi-scale modelling has gained considerable momentum for analysing mechanical response and failure of these heterogeneous materials with natural length scales [15–27]. Large domains can be effectively modelled by these techniques through different ways of information transfer between various scales. Methods for multi-scale analyses have been broadly classified into two groups. The first class of hierarchical models passes information from lower to higher scales through homogenization, usually in the form of material properties. The second class, known as concurrent methods, implements sub-structuring and concurrently solves different models at regions with different resolutions or scales. Two-way coupling of scales is enabled in the concurrent methods, which makes it suitable for problems involving localization, damage and failure [28]. Macroscopic analysis, using bottom-up homogenization in regions of homogeneous deformation enhances the efficiency of the computational analysis. On the other hand, the top-down localization process to cascade down to the microstructure in critical regions of localized damage, fracture or instability for pure microscopic analysis is necessary for achieving sufficient accuracy. A schematic of the concurrent multi-level computational approach, invoking bottom-up and top-down coupling, is shown in Figure 1. These microscopic computations, depicting the real microstructure are often complex and computationally prohibitive. The concurrent setting makes such analyses feasible, provided the ‘zoom-in’ regions are kept to a minimum.

An important challenge in the implementation of multiscale modelling method for structures constituted of non-uniform heterogeneous materials is the *a priori* delineation of morphological

DOI: 10.1002/nme

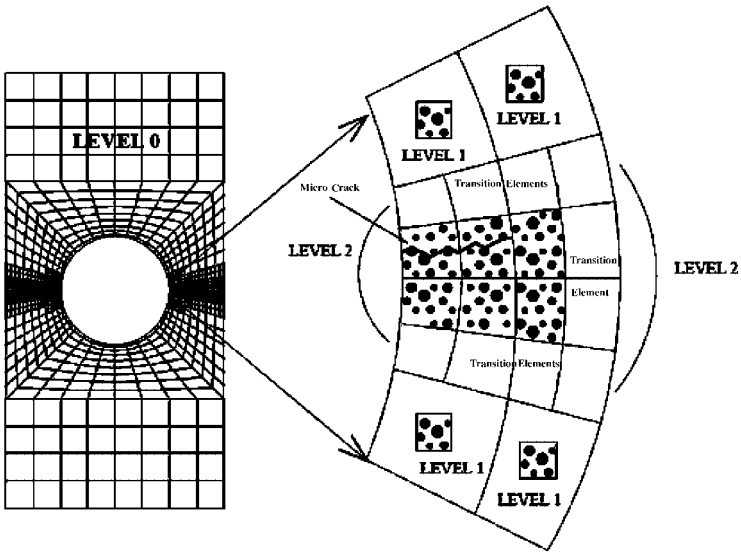

Figure 1. Schematic of a coupled concurrent multi-level model showing: (a) level-0 region of macroscopic continuum analysis with adaptive mesh refinement and zoom-in; and (b) blow-up of critical region containing level-1 (swing region with RVE analysis) and level-2 (region of pure micromechanical analysis).

information and properties at various scales. A few multi-scale models, e.g. References [16, 18, 29] have used a reasonably large number of inclusions ($\sim$100) in the microstructural representative volume, that are repeated everywhere. However in many heterogeneous materials, such repetitions are not realistic. In a concurrent macro–micro scale modelling approach, it is important that the starting computational domain be appropriately partitioned, based on information of the underlying microstructure. The morphology-based domain partitioning (MDP) should precede all concurrent multi-scale analyses, in which 'top-down' domain decomposition is based on evolving variables like stresses and strains. The MDP process is intended for two reasons: (i) to identify and determine microstructural representative material elements that can be used in the 'bottom-up' homogenization process for different regions in the overall computational domain and (ii) to identify those regions, where the morphology itself (e.g. regions of dense clustering) causes a breakdown in the assumptions of a homogenizable microstructure. These regions of microstructural analysis should then be embedded in complementary regions of homogenized macroscopic analysis in the concurrent model. The major ingredients of the MDP operation are generation of microstructure instantiations through image-based reconstruction methods, characterization or image analysis using known statistical functions and domain partitioning with criteria using these characterization functions.

Obtaining detailed microstructural information at all points in the structure is a non-trivial exercise and poses a major hurdle to experimental methods. Large domains demand large number of microstructural images, leading to challenges in their sequential acquisition by optical or scanning electron microscopy. A few methods have been suggested for dealing with this problem. A direct method of preparing a montage of a large number of high magnification microstructural images (nearly 400–500) followed by image compression has been proposed by Gokhale *et al.* [10, 30].

DOI: 10.1002/nme

This method, termed as the M-SLIP technique, is effective for small domains where few images are necessary. The microstructure information obtained has been shown to be sufficient for evaluating material's point statistics [31]. However, this process of experimentally extracting microstructural images at each individual point may be prohibitively exhaustive for large domains. The n-point statistics based stochastic image reconstruction techniques have also been used in practice. It involves generating characteristic functions of the morphology, e.g. the lineal path function, and using these functions to regenerate the microstructure through a process called simulated annealing or (SA). The (SA) method was introduced by Torquato *et al.* [32–34], in which a few pixels are randomly chosen for phase interchange in an iterative process. The interchange is retained based on the consequent change in a pseudo-energy variable that is expressed as a correlation function of the reconstructed image. While this method has the advantage of many correlation functions, it may need many iterations to evolve towards the expected microstructure and the convergence may not be achieved if the pseudo-cooling process for a certain acceptance rate is not appropriately scheduled. Due to its computational demand and convergence issues, its effectiveness for simulating large microstructural domains is still under investigation.

Other statistical methods of microstructure reconstruction that have been proposed, include random generation of points in a large domain [35] representing the centroids of heterogeneities followed by replacing each of these points with a heterogeneity of a definite shape. Since this generation is a completely random process, there is little possibility that the simulated microstructure can represent an actual microstructure to a high confidence level. Other similar methods include the random sequential packing algorithm (RSA) introduced in Reference [36] for simulating dispersions of regular shape heterogeneities and the Monte-Carlo technique in Reference [37]. Many of these stochastic methods suffer from slow convergence to the actual image. A few training-based techniques, like the example based super-resolution in Reference [38] have been proposed. High frequency bands of sample images at high resolution are used as training sets to enhance the interpolated image in these methods. However, they enhance surface textures rather than features associated with heterogeneities and also need an accompanying robust program for nearest neighbour search.

The present study is aimed at systematically creating a multi-scale image simulation–characterization methodology to enable domain partitioning as a pre-processor to multi-scale modelling of heterogeneous materials. The method, termed as MDP in this paper, is founded upon three sequential building blocks. The first step is to simulate necessary high-resolution microstructural information at all points of a computational domain from corresponding low resolution images of the domain and high resolution images at a few sample windows. Section 2 discusses these microstructure image representation and reconstruction techniques. The second step in Section 4 uses quantitative characterization of this high resolution microstructural information, e.g. phase distribution functions, to create effective metrics that can relate microstructural features to the material's physical behaviour. Such characterization is important in multi-scale modelling for establishing length scale characteristics at different resolutions. The third step, discussed in Section 5, invokes domain partitioning to delineate regions corresponding to different length scales in a coupled concurrent multi-scale model. Refinement functions are defined in terms of microstructural characteristics and these are used to adaptively create multi-level domain partitioning. The method developed in this paper is tested on a micrograph of a cast aluminium alloy A356 in Section 6. The method described here is for two-dimensional microstructures. Extension to 3D will involve additional methods for 3D data acquisition, as well as for 3D image processing and these are not addressed here.

DOI: 10.1002/nme

2. HIGH RESOLUTION MICROSTRUCTURE SIMULATION FROM LOW RESOLUTION IMAGES

A necessary requirement for creating a multi-scale domain partitioning of a heterogeneous computational domain is the knowledge of high-resolution microstructure at all points in the domain. Difficulties in experimentally obtaining contiguous high resolution microscopic images make the simulation or reconstruction of the local microstructure, highly desirable. These microstructures should be simulated from as few experimentally extracted micrographs as possible, and should replicate chosen morphological characteristics accurately. This section discusses a method for simulating these high resolution microstructures for all locations of a low resolution micrograph with information extracted from a few sample high resolution images. The techniques developed are applicable to optical microscopy or SEM-based micrographs of multi-phase materials like alloys, particle reinforced metal matrix composites, fibre reinforced polymer matrix composites, etc. The examples considered in this paper are for the cast Aluminium–Silicon alloy A356, which consists of low aspect-ratio eutectic Si and Al_2Cu, Fe–Mn-based intermetallics in the aluminium matrix. This material is used in the automotive industry for engine blocks, control arms, cross members, and cylinder heads. A typical low resolution image of A356 microstructure is shown in Figure 2. The image shows dark heterogeneities in grey aluminium matrix. The reconstruction process generates high resolution images with clear delineation of the multi-phase morphology needed for characterization and modelling.

A digital micrograph, such as the one in Figure 2, can be resolved into a grid of pixels with each pixel at a certain level in the greyscale (white–black) hierarchy. For a region Ω_{mic} in the micrograph containing $M \times N$ pixels, the greyscale level of a pixel at location (x, y) is represented by an indicator function $I^g(x, y) \in I$, where I is a space of integers. For a ζ-bit monochrome greyscale image, the function is defined as

$$I^g(x, y) = \{p : 0 \leqslant p \leqslant 2^{\zeta} - 1;\ \forall (1 \leqslant x \leqslant M); (1 \leqslant y \leqslant N) \in \Omega_{\text{mic}}\} \tag{1}$$

$I^g(x, y)$ can assume any integer value between 0 and 255 levels for a typical 8-bit monochrome image. A magnified image of a small region of micrograph is also shown in Figure 3(a). In this paper, magnification refers to the pixel size and hence a magnified image will have larger size of pixels with the same number of greyscale pixels as the original image. Resolution, on the other hand, corresponds to the number of pixels or pixel density in an image. Hence a higher resolution image will have a higher pixel density with associated greyscale levels. The number of pixels in the local image of Figure 3(a) is the same as that in the original image window of Figure 2, with bigger sized pixels. The magnified low resolution images contain fewer pixels than the high resolution counterparts, resulting in a loss of information. The microstructure reconstruction method is for extracting this additional information from consideration of a few non-contiguous high resolution images.

Various augmentation methods have been proposed in the literature. For example, sub-pixel value estimation in digital images by polynomial interpolation methods has been proposed in Reference [39]. This method does not consider simultaneous greyscale interpolation in orthogonal directions, and hence the images may be biased towards specific directions. Higher order interpolation techniques including the B-spline kernel method [40] provide more continuous representation of microstructural images, but the reconstructed micrographs are often blurred as shown in Figure 3(c). Directional methods that interpolate along the edges of heterogeneities rather than across them in Reference [41], reduce the blurring effect but require very high computational

DOI: 10.1002/nme

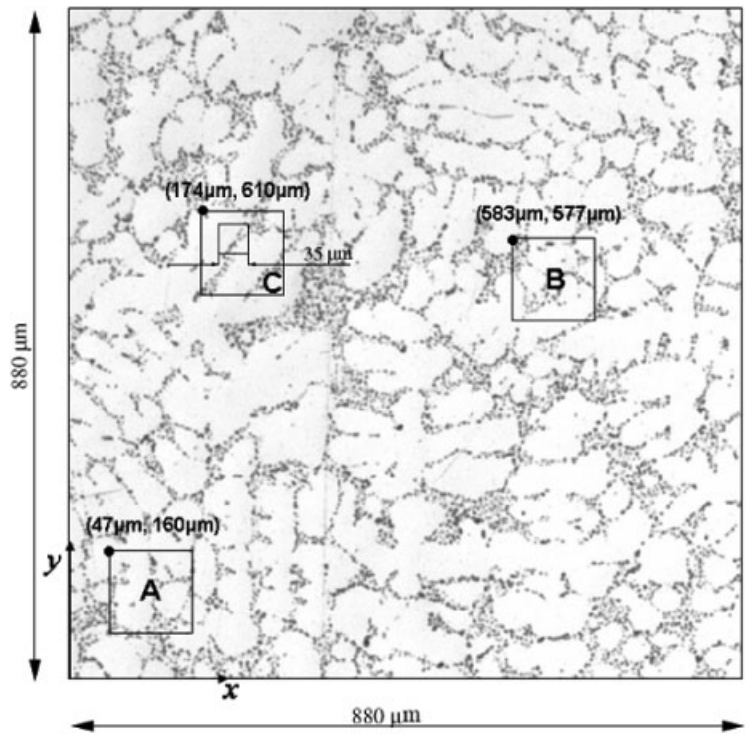

Figure 2. Low magnification, low resolution digital image of cast aluminium alloy A356, for which high resolution micrograph of a window C is desirable with available high resolution micrographs at other locations A and B.

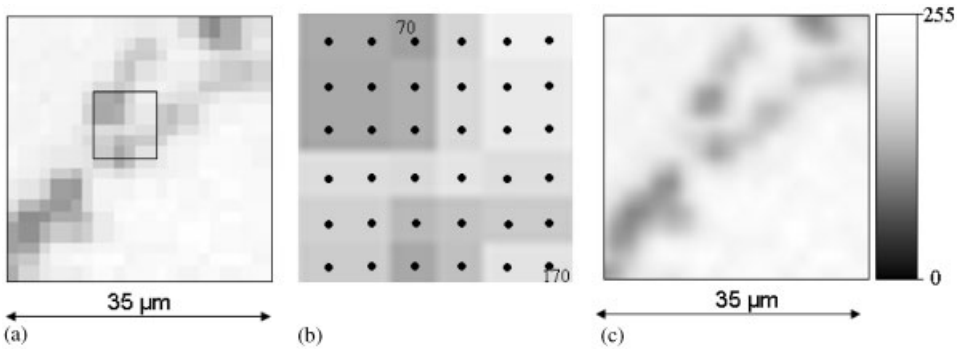

Figure 3. High magnification 35 μm × 35 μm images of a region near C, shown in Figure 2: (a) zoomed-in image showing larger pixels but with original resolution; (b) pixel representation of the square region marked in (a); and (c) a higher resolution micrograph of (a) obtained by interpolation.

DOI: 10.1002/nme

efforts. Wavelet-based local interpolation and augmentation of images has also been pursued in Reference [42]. In the present paper, low resolution image augmentation is accomplished by interpolation followed by gradient-based enhancement methods for creating higher resolution images. Two alternative microstructure regeneration methods are introduced in the following subsections.

2.1. Polynomial interpolation with greyscale based enhancement (PIGE) algorithm

In this method, the integer indicator function $I^g(x, y)$ is first interpolated in real space using a polynomial surface interpolation function. Let a window Ω_w^{lrsm} of the low resolution image encompass a $p \times q$ pixel grid, while the same window for a higher resolution image Ω_w^{hrsm} be represented by a $p' \times q'$ pixel grid, where $p' > p$ and $q' > q$. The greyscale level of each pixel in the $p \times q$ pixel grid is represented by the value of the indicator function $I^g(x, y)$ at its centroid. Hence, $I^g(x, y)$ has known values at a set of equi-spaced points in the low resolution image window as shown in Figure 3(b). Interpolation is used for estimating the indicator functions ($I^{g'}(x, y) \in R$) in the high resolution $p' \times q'$ pixel grid, where R is the space of real numbers bounded by 0 and 255. Polynomial based interpolation methods in Reference [39] have been used as a one-dimensional convolution over the micrograph, where interpolations are performed along horizontal and vertical directions separately, resulting in a loss of spatial correlation. A higher order polynomial surface is used in this work to interpolate the indicator function $I^{g'}(x, y)$ in the $p' \times q'$ pixel grid Ω_w^{intm} as

$$\begin{aligned} I^{g'}(x, y) &= (A_0 + A_1 x + A_2 x^2 + \cdots + A_{p-1} x^{p-1}) \times (B_0 + B_1 y + B_2 y^2 + \cdots + B_{q-1} y^{q-1}) \\ &= C_0 + C_1 x + C_2 y + \cdots + C_{pq-1} x^{p-1} y^{q-1} \end{aligned} \tag{2}$$

The coefficients $C_0, C_1, \ldots, C_{pq-1}$ are obtained by substituting the values of $I^g(x, y)$ for the centroids of each pixel in the $p \times q$ grid and solving the set of pq linear equations

$$I^g(x_i, y_i) = C_0 + C_1 x_i + C_2 y_i + \cdots + C_{pq-1} x_i^{p-1} y_i^{q-1} \quad \forall 1 \leqslant i \leqslant pq \tag{3}$$

or in a matrix form

$$\{\mathbf{I}^{g'}\} = [\mathbf{F}]\{\mathbf{C}\} \tag{4}$$

where $\{\mathbf{I}^g\}$, $[\mathbf{F}]$ and $\{\mathbf{C}\}$ are matrices of order $pq \times 1$, $pq \times pq$ and $pq \times 1$, respectively. The matrix $\{\mathbf{I}^g\}$ is similar to the Vandermonde matrix of 1-dimensional polynomial interpolation. From a numerical standpoint, very large numbers for p and q lead to instability in the solution of coefficients, due to nearly linearly dependent columns in $[\mathbf{F}]$. Numerical studies conducted indicate that the values for which the system is stable are around $p = 6$, $q = 6$. Consequently the low resolution image is subdivided into basic building blocks containing a maximum of 6×6 pixels. The overall $I^{g'}(x, y)$ for the window containing a $p' \times q'$ pixel grid is therefore constructed as a piecewise continuous function, using the interpolation equation (2) in each block. For each block, (x, y) can represent co-ordinates in a local co-ordinate system with the origin located at the centroid of the block. Consequently, for all blocks of the same dimension, e.g. 6×6, the matrix $[\mathbf{F}]$ in Equation (4) will be the same. Hence the matrix and its inverse need to be computed only once, irrespective of the size of the image to be reconstructed.

The interpolation method is tested on a window marked B in the low resolution A356 micrograph of Figure 2. The dimensions of the entire micrograph and the window are 880 μm × 880 μm

DOI: 10.1002/nme

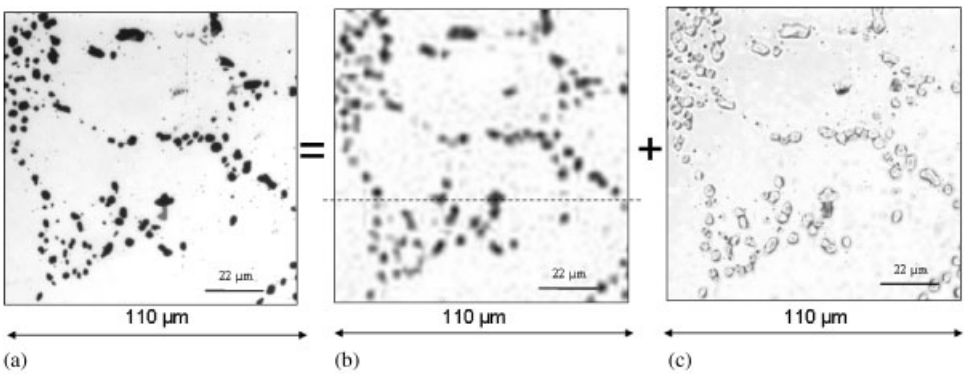

Figure 4. High resolution micrographs at location B in Figure 2: (a) actual high resolution micrograph; (b) micrograph obtained by polynomial interpolation in the PIGE algorithm; and (c) difference micrograph between (a) and (b).

and 110 μm × 110 μm, respectively. The magnified low resolution interpolated image consists of $60(=p) \times 60(=q)$ pixel grid. Hence there are 10×10 blocks containing 6×6 pixel grids each, in this window. A high resolution SEM micrograph at the same exact location is shown in Figure 4(a), which has a $480(=p') \times 480(=q')$ pixel grid, corresponding to a 64-fold increase in pixel density. The interpolated image, obtained by applying Equation (2) to the low resolution image should have the same pixel density as the high resolution image. This is depicted in Figure 4(b) on the 480×480 pixel grid. Interpolation smoothens all sharp edges of the low magnification image and these manifest as blurred edges in the simulated micrograph. A pixel by pixel subtraction of image 4(b) indicator functions from those for image 4(a) is depicted in Figure 4(c). It is clear from the difference figure that interpolation alone does not suffice for achieving an accurate high resolution microstructure reconstruction. This necessitates an image enhancement process following interpolation.

2.1.1. Post interpolation enhancement. An enhancement method is proposed to augment the interpolated images of low resolution micrographs, from pixel data of a few high resolution images. The method accounts for the proximity of calibrating micrographs to those being simulated. The first step in this process is the pixel by pixel determination of the difference in the image indicator function values between the high resolution scanning or optical micrographs Ω_w^{hrsm} and the interpolated microstructural image Ω_w^{intm} in the high density pixel grid. This is expressed as

$$I_{\text{diff}}^{g'}(x, y) = I_{\text{hrsm}}^{g'}(x, y) - I_{\text{intm}}^{g'}(x, y) \tag{5}$$

The difference micrograph Ω_w^{diff} between images 4(a) and (b) is shown in Figure 4(c).

The augmentation methodology requires the creation of a correlation map between $I_{\text{diff}}^{g'}(x, y)$ and $I_{\text{intm}}^{g'}(x, y)$ that will predict the high resolution image Ω_w^{hrsm} from specific features of the interpolated image Ω_w^{intm}. For the interpolated image, the pixel-wise grey-scale level or indicator function as well as its gradients, are considered to be characteristic variables that are representative of the local phase distribution. At a point in the pixel space, the value of $I_{\text{intm}}^{g'}(x, y)$ itself is an

DOI: 10.1002/nme

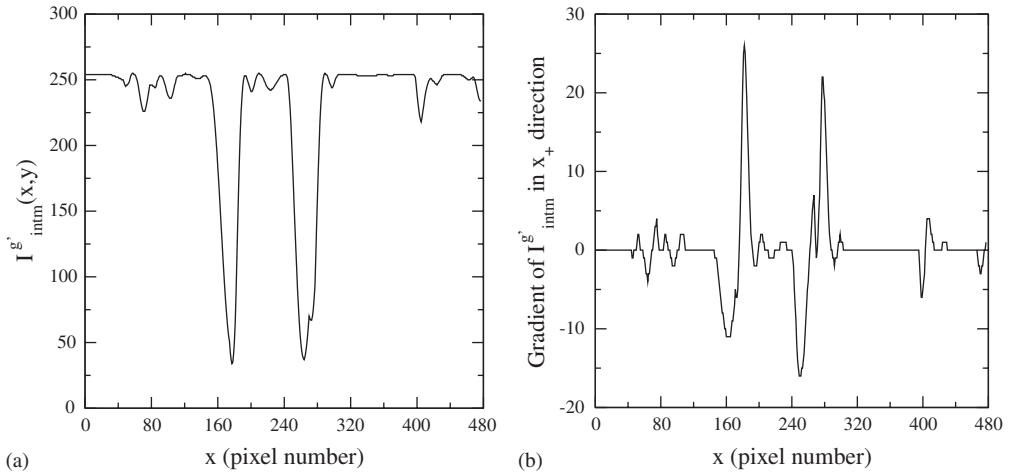

Figure 5. (a) Pixel greyscale value; and (b) grey-scale gradient along the dotted line in the interpolated micrograph of Figure 4(b).

indicator of a given phase. Gradients of the indicator in the four directions (x_+, x_-, y_+, y_-), on the other hand, refer to its extent and the neighbourhood. Figures 5(a) and (b) show the plots of $I^{g'}_{\text{intm}}(x, y)$ and its gradient in the x_+ direction along the dotted line in Figure 4(b). Both the indicator function and its gradient show major peaks in the same regions and reduce sharply near the boundaries of the second phase inclusions. A discrete correlation function is created between these characteristic variables of the interpolated image Ω^{intm}_w and the indicator function value $I^{g'}_{\text{diff}}(x, y)$ of the difference image Ω^{diff}_w, for locations where high resolution calibrating micrographs are available. The probability or correlation map may be expressed in a functional form of the indicator function and its gradients as

$$I^{g'}_{\text{diff}}(x, y) = P_{\text{diff}}\left(I^{g'}_{\text{intm}}(x, y), \frac{\partial I^{g'}_{\text{intm}}}{\partial x_+}, \frac{\partial I^{g'}_{\text{intm}}}{\partial x_-}, \frac{\partial I^{g'}_{\text{intm}}}{\partial y_-}, \frac{\partial I^{g'}_{\text{intm}}}{\partial y_+}\right) \tag{6}$$

where P_{diff} corresponds to the most probable or expected value of the difference indicator function and

$$\begin{aligned} \frac{\partial I^{g'}_{\text{intm}}}{\partial x_\pm} &= \frac{I^{g'}_{\text{intm}}(x \pm NG, y) - I^{g'}_{\text{intm}}(x, y)}{NG} \\ \frac{\partial I^{g'}_{\text{intm}}}{\partial y_\pm} &= \frac{I^{g'}_{\text{intm}}(x, y \pm NG) - I^{g'}_{\text{intm}}(x, y)}{NG} \end{aligned} \tag{7}$$

NG is the number of pixels over which the gradient is evaluated. The functional form of P_{diff} is not known *a priori*. Hence a discrete probability table is constructed from the calibration micrographs Ω^{intm}_w and Ω^{diff}_w to construct this correlation map. A schematic of the probability table is shown in Figure 6. The table is partitioned into discrete boxes or 'bins', based on ranges of $I^{g'}_{\text{intm}}$ and

DOI: 10.1002/nme

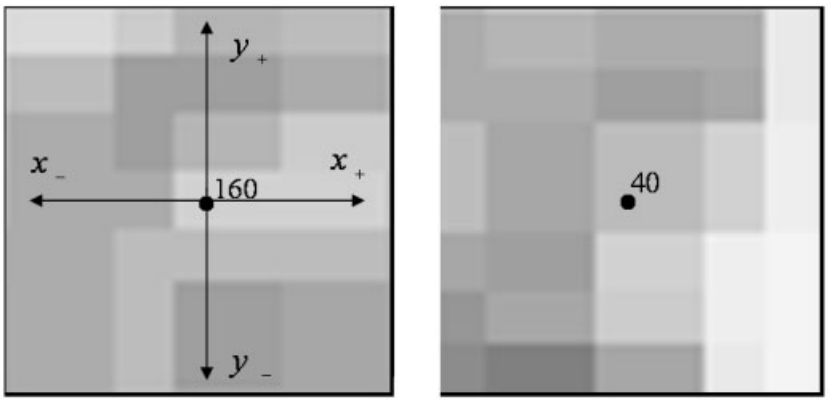

(a) (b)

$I^{g'}_{intm}$	0-25	25-50	50-100	100-125	125-150	150-175	...	225-255
$\lvert(I^{g'}_{intm})_{,x+}\rvert$: 0-7 $\lvert(I^{g'}_{intm})_{,x-}\rvert$: 0-7 $\lvert(I^{g'}_{intm})_{,y+}\rvert$: 0-7 $\lvert(I^{g'}_{intm})_{,y-}\rvert$: 0-7						$I^{g'}_{diff}$=40		
$\lvert(I^{g'}_{intm})_{,x+}\rvert$: >7 $\lvert(I^{g'}_{intm})_{,x-}\rvert$: 0-7 $\lvert(I^{g'}_{intm})_{,y+}\rvert$: 0-7 $\lvert(I^{g'}_{intm})_{,y-}\rvert$: 0-7								
...								
$\lvert(I^{g'}_{intm})_{,x+}\rvert$: >7 $\lvert(I^{g'}_{intm})_{,x-}\rvert$: >7 $\lvert(I^{g'}_{intm})_{,y+}\rvert$: >7 $\lvert(I^{g'}_{intm})_{,y-}\rvert$: >7								

(c)

Figure 6. Method of correlating interpolated and difference micrographs: (a) a polynomial interpolated region; (b) corresponding difference region; and (c) table with bins correlating the interpolated micrograph with the difference micrograph.

its gradients in four directions, i.e. $\partial I^{g'}_{\text{intm}}/\partial x_+$, $\partial I^{g'}_{\text{intm}}/\partial x_-$, $\partial I^{g'}_{\text{intm}}/\partial y_-$, $\partial I^{g'}_{\text{intm}}/\partial y_+$ in Ω^{intm}_w. The gradients in the bins are expressed with the notation $\partial I^{g'}_{\text{intm}}/\partial x_+ = (I^{g'}_{\text{intm}})_{,x+}$ and so on.

Each bin is represented by a range of values for each of the five variables, and contains the values of difference indicator function $I^{g'}_{\text{diff}}$ in the difference image Ω^{diff}_w. The range of values of the variables in each bin is assigned from consideration of their variability. For example, the range

DOI: 10.1002/nme

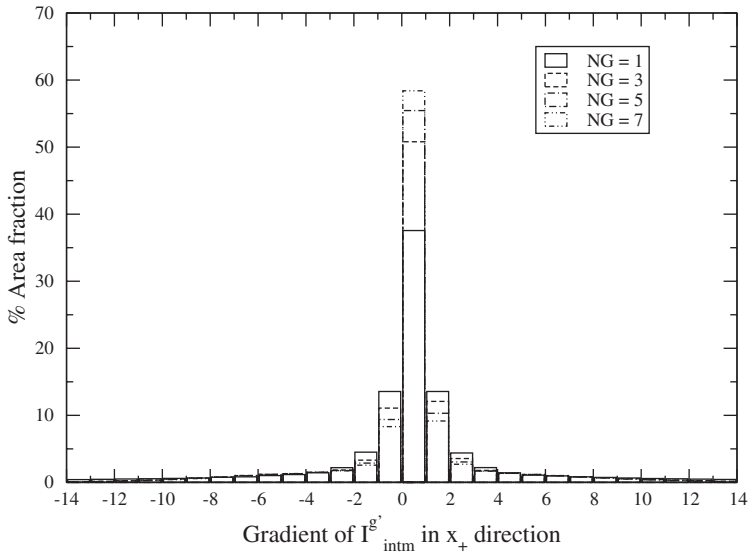

Figure 7. Distribution histogram of the indicator function gradient $\partial I^{g'}_{\text{intm}}/\partial x_+$ in the interpolated image of Figure 4(b) for various values of *NG*.

of the indicator value $0 \leqslant I^{g'}_{\text{intm}} \leqslant 255$ can be divided into as high as 256 bins or as low as 2–3 bins. However with increasing number of bins, the number of $I^{g'}_{\text{diff}}$ entries in each bin will decrease and many of the bins may be empty for the calibration micrographs considered. Sparsity in the correlation bins renders the reliability of this probability table to be low. A moderate number of divisions (10–15) is numerically found to be sufficient in this paper, as corroborated by convergence studies discussed later. The range of divisions in the gradients should be such that they are able to distinguish between regions that belong to the interior and exterior of a given phase. A histogram of the distribution in area fraction of the gradient $\partial I^{g'}_{\text{intm}}/\partial x_+$ for different pixel offset values *NG* in the image 4(b) is plotted in Figure 7. It is evident that the gradient distribution is independent of the number *NG* used in Equation (7). A value of $NG = 1$ is used in this work. Another observation is that the area fraction within the bounds $-7 \leqslant \partial I^{g'}_{\text{intm}}/\partial x_+ \leqslant 7$ corresponds to the inclusions in the microstructure. This conforms to the requirement of delineating regions that belong inside of the inclusion phase. Consequently, the range of values for the gradient is divided into two groups: (i) $|\partial I^{g'}_{\text{intm}}/\partial x_+| < 7$ and (ii) $|\partial I^{g'}_{\text{intm}}/\partial x_+| \geqslant 7$. The same division is applicable to gradients in other directions too. Figure 6(c) shows the probability table with the discretized ranges of indicator function and its gradients. At a given pixel in Ω^{intm}_w of Figure 6(a), $I^{g'}_{\text{intm}} = 160$, $\partial I^{g'}_{\text{intm}}/\partial x_+ = 4.0$, $\partial I^{g'}_{\text{intm}}/\partial x_- = 5.0$, $\partial I^{g'}_{\text{intm}}/\partial y_+ = 5.5$, and $\partial I^{g'}_{\text{intm}}/\partial y_- = 4.5$. The corresponding $I^{g'}_{\text{diff}} = 40$ is inserted in the probability Figure 6(c). The values of $I^{g'}_{\text{diff}}$ in the correlation bins vary from location to location for different samples. A histogram of the distribution of $I^{g'}_{\text{diff}}$ for a given bin corresponding to $(0 \leqslant I^{g'}_{\text{intm}} < 25, |\partial I^{g'}_{\text{intm}}/\partial x_+| < 7, |\partial I^{g'}_{\text{intm}}/\partial x_-| < 7, |\partial I^{g'}_{\text{intm}}/\partial y_+| < 7, |\partial I^{g'}_{\text{intm}}/\partial y_-| < 7)$ is shown in Figure 8. The peaks in the histogram associate a high probability value of $I^{g'}_{\text{diff}}$ with that correlation

DOI: 10.1002/nme

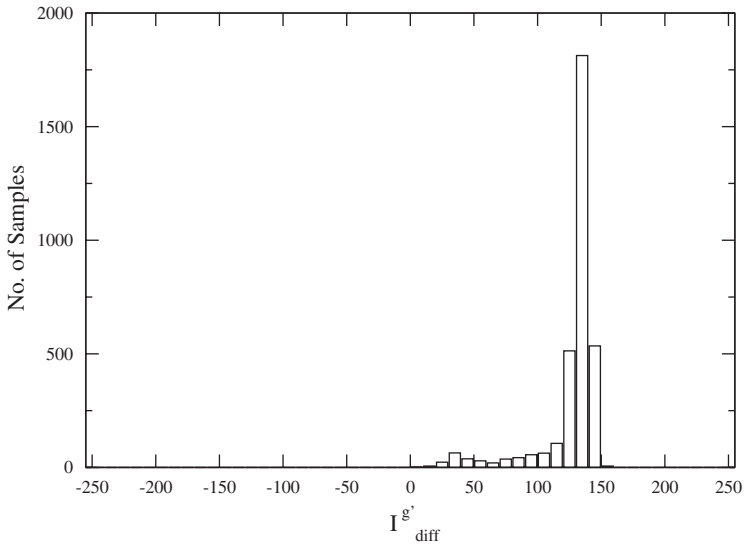

Figure 8. A histogram of the distribution of $I_{\text{diff}}^{g'}$ in the difference image for a given bin corresponding to $(0 \leqslant I_{\text{intm}}^{g'} < 25, |\partial I_{\text{intm}}^{g'}/\partial x_+| < 7, |\partial I_{\text{intm}}^{g'}/\partial x_-| < 7, |\partial I_{\text{intm}}^{g'}/\partial y_+| < 7, |\partial I_{\text{intm}}^{g'}/\partial y_-| < 7)$.

bin. This corresponds to the expected value of $I_{\text{diff}}^{g'} = P_{\text{diff}}(I_{\text{intm}}^{g'}, \partial I_{\text{intm}}^{g'}/\partial x_+, \ldots)$ that is selected for image enhancement of $I_{\text{intm}}^{g'}$ according to Equation (5).

The location of the high resolution calibrating micrograph in relation to that of the image being simulated is of considerable importance in the image augmentation process. It is assumed that the calibrating micrographs contain the same constituent phase materials as the ones being simulated and they are both produced in the same batch by the same manufacturing process. As a consequence, the probability or expected value of difference indicator functions in Equation (6) may be assumed to have a continuous variation from one micrograph to the next. This assumption is important for incorporating the effect of location in the calibration process. For sharply contrasting micro-regions, calibrating micrographs should be appropriately chosen from regions that represent the essential features of the one being simulated. The effect of proximity between the calibrating and simulated images can be addressed by assigning distance-based weights to the expected values in the probability table. Micrographs closer to the simulated image will have a stronger influence than those that are farther away. The inverse dependence of a microstructure's correlation map on its spatial distance from each of the calibrating micrographs is represented by a 'shape function' type interpolation relation, commonly used in finite element analysis, i.e.

$$P_{\text{diff}}(x, y) = \sum_{\alpha} N_{\alpha}(x, y) P_{\text{diff}}(x_{\alpha}, y_{\alpha}) \tag{8}$$

where α is the total number of high resolution calibration micrographs and N_{α} are the associated shape functions. When only two calibrating micrographs A and B are available as in Figure 2, the most expected value of the enhancement $I_{\text{diff}}^{g'}(x, y)$ at a pixel in the simulated micro-image is

DOI: 10.1002/nme

given as

$$I^{g'}_{\text{diff}}(x, y) = P_{\text{diff}}(x, y) = \left(\frac{1-\xi}{2}\right) P_{\text{diff}}(x_A, y_A) + \left(\frac{1+\xi}{2}\right) P_{\text{diff}}(x_B, y_B) \tag{9}$$

Here $\xi = ((R_A - R_B)/R_{AB})$ and R_A and R_B are the distances of a pixel in the simulated image from the corresponding pixels in calibrating micrographs A and B, respectively, and R_{AB} is the distance between them. For microstructures containing a single predominant inclusion phase in the matrix, e.g. the Si phase for the cast aluminium alloy A356, the various locations A and B may be statistically equivalent with respect to the pixel-based expected value in the probability table of Figure 6(c). In this case, the effect of multiple locations (e.g. A, B, etc.) in Equation (9) may be minimal.

The effectiveness and convergence characteristics of the PIGE algorithm are tested by comparing characteristic metrics of the simulated microstructure with those for an experimentally acquired micrograph at the same location. The n-point statistics [43] are effective metrics for multi-phase microstructure characterization and are used in this study as validation tools. Specifically, the 1-point, 2-point and 3-point statistics are used for this validation. For the low resolution microstructural region of Figure 2, windows at locations A and B are the high resolution calibration micrographs. The PIGE algorithm simulates the image at a window C, for which a high resolution SEM micrograph is available for validation. The 1-point probability function corresponds to the area fraction of the second phase inclusions. Its variation is plotted in Figure 9 as a function of increasing number of divisions in the range of $I^{g'}_{\text{intm}}$, called bins in the probability table. The simulated area fraction converges to the SEM image area fraction with about 8 discrete divisions or bins. The 2-point probability function is defined as the probability of finding two points at

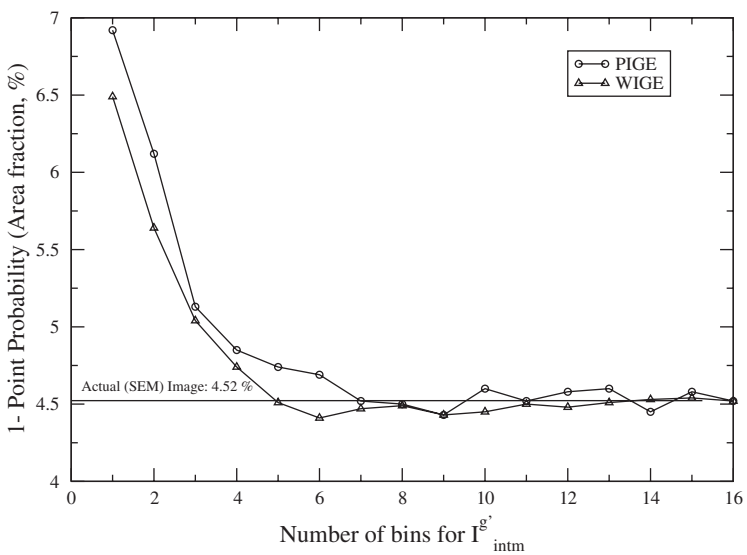

Figure 9. Convergence of 1-point probability function with increasing number of divisions in the range of $I^{g'}_{\text{intm}}$ or bins, for the simulated micrograph at region C of Figure 2 by the PIGE and WIGE methods.

DOI: 10.1002/nme

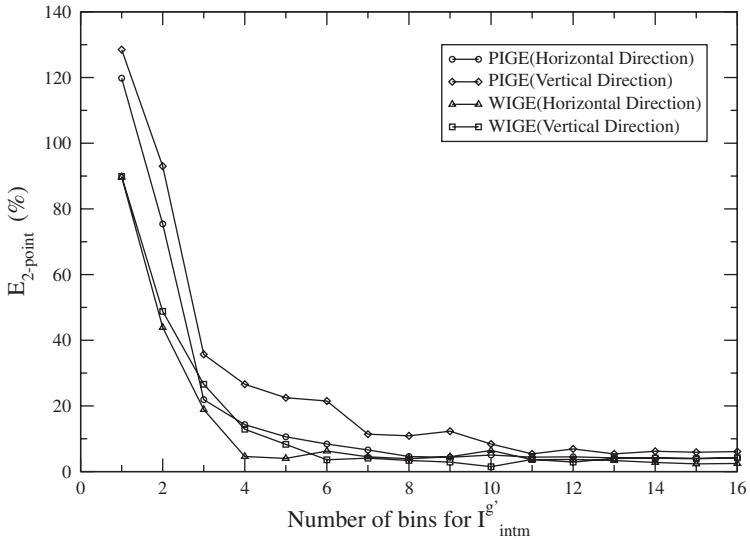

Figure 10. Convergence of 2-point probability function with increasing number of divisions in the range of $I_{\text{intm}}^{g'}$ or bins, for the simulated micrograph at region C of Figure 2 by the PIGE and WIGE methods.

$r_1(x_1, y_1)$ and $r_2(x_2, y_2)$ (end-points of a line) separated by a distance $r = r_1 - r_2$ in the same phase in the material microstructure, i.e.

$$P_{ij}(r) = P\{I^b(x_1, y_1) = 1, I^b(x_2, y_2) = 1\}$$
$$\text{where } I^b = 1 \text{ in the given phase and } I^b = 0 \text{ otherwise} \tag{10}$$

The % error in the 2-point probability function between the actual and simulated images is defined as

$$E_{2\text{-point}} = \frac{\sum_{r=0}^{r=L/2} |P_{ij}^{\text{SEM}} - P_{ij}^{\text{sim}}|}{\sum_{r=0}^{r=L/2} P_{ij}^{\text{SEM}}} \times 100\% \tag{11}$$

This error is evaluated along the two orthogonal directions and plotted in Figure 10. Once again, a fast convergence is noted and the error stabilizes to a near zero value with around 10 bins. Finally, the 3-point probability function is defined as the probability of finding three points at $r_1(x_1, y_1)$, $r_2(x_2, y_2)$ and $r_3(x_3, y_3)$ (vertices of a triangle) in the same phase, i.e.

$$P_{ijk}(r) = P\{I^b(x_1, y_1) = 1, I^b(x_2, y_2) = 1, I^b(x_3, y_3) = 1\} \tag{12}$$

$P_{ijk}(r)$ is evaluated for three points at the vertices of an isosceles right triangle with interior angles 45°, 45°, 90°. The error in the 3-point probability function is defined in the same way as in Equation (11) and is plotted in Figure 11. The error in the 3-point probability function also stabilizes to near zero values with around 10 bins. The lower order statistics provide information on phase dispersion and are relevant to domain partitioning. Higher order statistics like the 3-point probability function are important with respect to phase shapes that control the localization and

DOI: 10.1002/nme

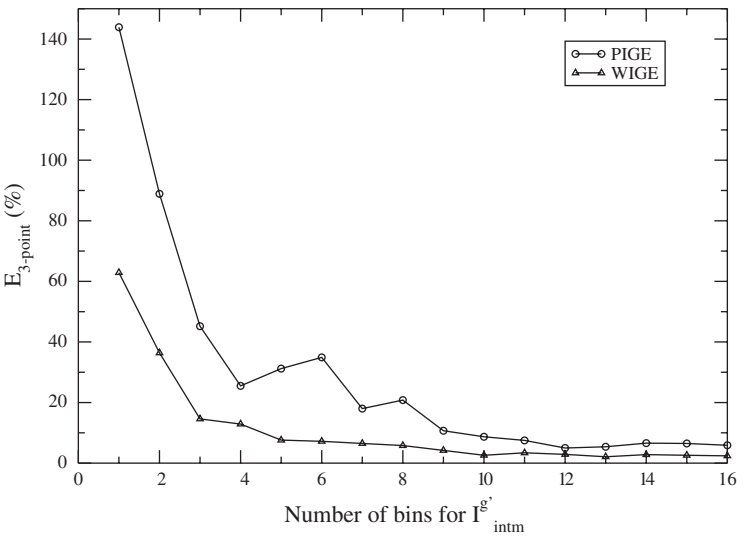

Figure 11. Convergence of 3-point probability function with increasing number of divisions in the range of $I^{g'}_{\text{intm}}$ or bins, for the simulated micrograph at region *C* of Figure 2 by the PIGE and WIGE methods.

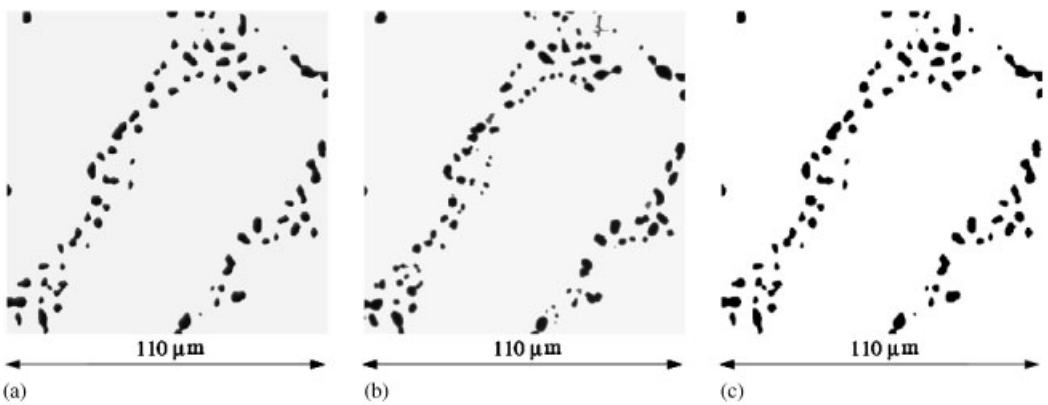

Figure 12. High resolution micrograph at location *C* of Figure 2 by the PIGE algorithm: (a) simulated micrograph by using the correlation table; (b) the real high resolution micrograph; and (c) binary high resolution micrograph.

damage behaviour of the material. It may be concluded that the convergence characteristics of the PIGE algorithm is quite satisfactory with respect to the error in 1-point, 2-point and 3-point statistics. The PIGE simulated microstructural image and the corresponding actual micrograph are shown in Figures 12(a) and (b). Thus the PIGE algorithm can be applied sequentially to all windows in the computational domain for obtaining high resolution images.

DOI: 10.1002/nme

2.2. *Wavelet based interpolation with gradient based enhancement (WIGE) algorithm*

Wavelet basis functions are also good candidates for image reconstruction due to their exceptional capability of capturing sharp variations in microstructure images [44, 45]. Multi-resolution properties of wavelets enable pyramidal decomposition of image data that can be applied towards image compression. In the wavelet based image decomposition technique, the digital image with pixels is encoded using wavelet basis functions constructed about the centre of each pixel. The low resolution image can be encoded with a combination of wavelet functions, each defined about the centre of each pixel in the domain. The corresponding high resolution images are simulated from the difference between the wavelet interpolated low resolution images and actual high resolution micrographs. For image compression in Reference [42], only significant values of the difference image have been stored or further encoded, eventually resulting in a pyramidal decomposition. Image reconstruction by the WIGE algorithm involves (a) constructing an interpolated image in a high-density pixel mesh using wavelet functions, (b) delineating the corresponding difference image, and (c) creating a correlation map for each pixel in the difference image in terms of characteristic variables at the corresponding pixel of the interpolated image, similar to that in the PIGE algorithm in Section 2.1. High resolution images can then be constructed for all points of the low resolution micrographs with these correlation functions. An advantage with the wavelet-based interpolation is that discontinuities in the microstructural phases can be represented well and hence the indicator function gradients in the probability table can be more meaningful.

Gaussian functions with continuous derivatives are popular wavelets bases [46, 47] and can effectively represent sharp variations in image features. This function is of the form

$$\Phi_{m,n,k,l}(x, y) = \mathrm{e}^{-1/2((x-b_n)/a_m)^2} \mathrm{e}^{-1/2((y-d_l)/c_k)^2} \beta_{m,n,k,l} \tag{13}$$

where (m, k) refer to the wavelet level, (n, l) correspond to the discrete translation of the bases in x and y directions, respectively, with b_n, d_l as the translation parameters, and a_m, c_k are dilation parameters. In encoding a $p \times q$ pixel sub-region of a low resolution image, the indicator function is expressed in terms of the level (m, k) Gaussian wavelet function as

$$I^{g'}_{\mathrm{wvlt}}(x, y) = \sum_{1 \leqslant i \leqslant p} \sum_{1 \leqslant j \leqslant q} \Phi_{m,i,k,j}(x, y) \tag{14}$$

This yields a continuous interpolated image representation in terms of indicator function from the low resolution image. The bases are constructed by translation from one pixel to the next in the $p \times q$ pixel sub-region and the region is encoded with $p \times q$ Gaussian functions. At locations where high resolution SEM micrographs are available, the difference image is obtained and the correlation is constructed as

$$I^{g'}_{\mathrm{hrsm}}(x, y) - I^{g'}_{\mathrm{wvlt}}(x, y) = I^{g'}_{\mathrm{diff}}(x, y) = P_{\mathrm{diff}}\left(I^{g'}_{\mathrm{wvlt}}(x, y), \frac{\partial I^{g'}_{\mathrm{wvlt}}}{\partial x_+}, \frac{\partial I^{g'}_{\mathrm{wvlt}}}{\partial x_-}, \frac{\partial I^{g'}_{\mathrm{wvlt}}}{\partial y_-}, \frac{\partial I^{g'}_{\mathrm{wvlt}}}{\partial y_+}\right) \tag{15}$$

where P_{diff} is the expected value of difference indicator function, defined in Equation (7). As in the PIGE algorithm, the expected values are extracted from a correlation map between interpolated and difference images built as a discrete function table of Figure 6. This correlation function expresses the difference indicator function $I^{g'}_{\mathrm{diff}}(x, y)$ in terms of the wavelet-interpolated image indicator function $I^{g'}_{\mathrm{wvlt}}(x, y)$ and its gradients in the four directions $\partial I^{g'}_{\mathrm{wvlt}}/\partial x_{+/-}$ and $\partial I^{g'}_{\mathrm{wvlt}}/\partial y_{+/-}$.

DOI: 10.1002/nme

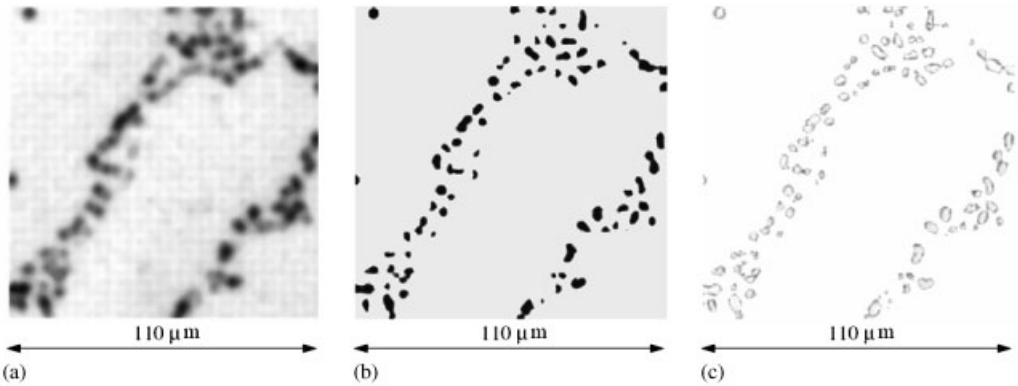

Figure 13. High resolution micrographs at location C in Figure 2 by the WIGE method: (a) wavelet interpolated micrograph; (b) interpolated micrograph with enhancement; and (c) difference between the simulated micrograph in (b) and actual micrograph in Figure 12(b).

Following the calibration of simulated micrographs, high resolution microstructural images are simulated at any location of the low resolution micrograph using the WIGE algorithm and spatial interpolation relation of Equation (9). The post-interpolation image enhancement procedure closely follows the PIGE algorithm discussed in Section 2.1.

The WIGE algorithm is tested for the same cast alloy A356 microstructure of Figure 2. The basic blocks in this construction have a pixel density $6(=p) \times 6(=q)$ and the high resolution blocks have a density of $48(=p') \times 48(=q')$. This corresponds to a 64-fold increase in pixel density. The resulting interpolated image and the high resolution simulated image are shown in Figures 13(a) and (b). Also the difference between the enhanced simulated image and the corresponding SEM image for location C is shown in Figure 13(c). The difference image shows very good concurrence between the simulated and real images. Again the n-point statistics of the simulated image are compared with that of the SEM micrograph. The 1-point, 2-point and 3-point statistics are plotted in Figures 9, 10 and 11, respectively. At the converged state, the error in these probability functions are less than 1% (for 1-point probability), 2.48% (for 2-point probability in x direction), 4.21% (for 2-point probability in y direction), and 2.4% (for 3-point probability), respectively. The plots clearly show that the convergence rates with the WIGE algorithm are better than those with the PIGE algorithm. This is due to the fact that gradients of the indicator functions, corresponding to sharp gradients in the image pixel grey-scale levels, are better represented by the former algorithm.

3. MICROSTRUCTURAL IMAGE PROCESSING AND BINARY IMAGES

Prior to characterizing the microstructure of the entire simulated computational domain, it is necessary to process these images to eliminate noise and clearly delineate dominant phases. Hierarchy in the greyscale levels of digital images is used for such image processing. During phase delineation, the indicator function values $I^g(x, y)$ of all pixels belonging to a given phase are assumed to fall within a narrow band of greyscale levels. Global thresholding is first conducted to enable phase delineation or segmentation in the micrographs. In global thresholding, $I^g(x, y)$ is

DOI: 10.1002/nme

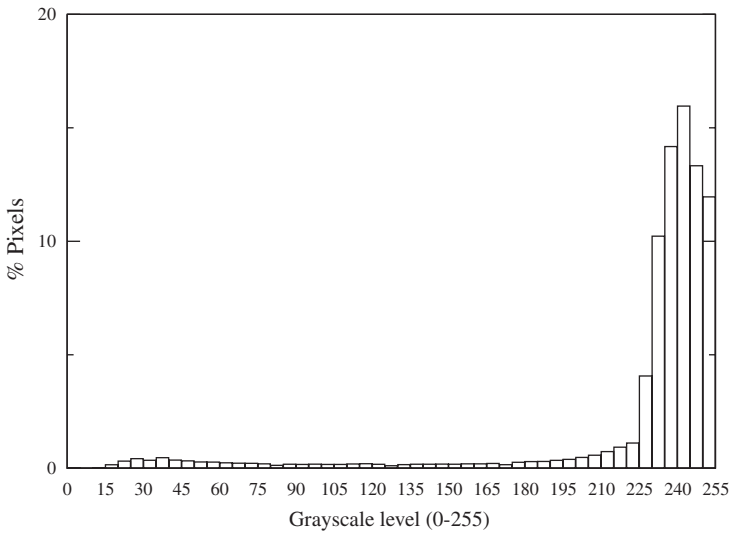

Figure 14. Brightness histogram of high resolution micrograph in Figure 12(a).

binarized for the entire image with respect to a single threshold value. On the other hand, different values may be used in local thresholding based on the local variation of $I^g(x, y)$. The latter may be necessary for those micrographs, where the same phase may have large differences in greyscale level representations at different locations. Global thresholding is deemed sufficient in this work, since the range of greyscale levels of each phase is assumed to have a narrow bandwidth. In a perfect image belonging to two distinct greyscale levels, global thresholding will yield a bimodal histogram of the percentage of pixels as a function of the greyscale levels. Two distinct peaks exist for such a bimodal histogram and the threshold value of $I^g(x, y)$ corresponds to the valley point between the peaks. Some of the relevant techniques for processing such images have been presented in Reference [11]. However, in real images such as in Figure 14, bimodal histograms are rarely observed. Various techniques have been suggested in the literature for evaluating the threshold value τ in histograms without distinct peaks [48, 49]. A simple technique is to evaluate τ from the shoulder region in the histogram adjacent to the peak for the matrix phase that has a zero slope. The image can be binarized with respect to the indicator function value as

$$\begin{aligned} I^b(x, y) &= 1 \quad \forall 0 \leqslant I^g(x, y) \leqslant \tau \\ &= 0 \quad \forall \tau < I^g(x, y) \leqslant 2^\zeta - 1 \end{aligned} \tag{16}$$

Heterogeneities (inclusions or voids) are consequently converted to a black image against a white matrix backdrop. For the A356 micrograph of Figure 4(a), a threshold value of $\tau = 225$ is obtained from the histogram in Figure 14. The corresponding binary (black and white) image of the microstructure is shown in Figure 12(c). For multi-phase materials (more than two phases), more than one threshold is necessary to separate different phases in the microstructure. The distinction between Si particles and intermetallics in cast A356 is not made in the present work, since the focus is on morphology of additional phases for geometry-based image processing. Such distinction can be enforced when material properties are of consequence.

DOI: 10.1002/nme

Quite often, micrographs have significant noise due to tiny erroneous marks. The corresponding indicator functions $I^g(x, y)$ get transferred to the binary image indicators $I^b(x, y)$ based on their greyscale value. To prevent this, $I^g(x, y)$ is convoluted with a mean filter of mask size n as shown in Reference [50]. The process replaces each pixel at (x, y) with its respective local average greyscale level. The binary image also often contains tiny speckles due to thresholding, which are unwanted noise. The binary image is despeckled using a median filter on a kernel of mask size m pixels. The de-noising kernels help the automation of the whole process without any user intervention. The binary domain, derived from this process, represents a high resolution computational domain Ω_{mic} necessary for microstructural characterization and analysis. It is the union of regions belonging to the matrix phase $\{\Xi_m\}$ and the N_c heterogeneities, represented as $\{\Xi_c^i : 1 \leqslant i \leqslant N_c\}$, i.e. $\Omega_{\text{mic}} = \Xi_m + \sum_{i=1}^{N_c} \Xi_c^i$.

4. MICROSTRUCTURE CHARACTERIZATION FUNCTIONS

Characterization is essential for quantifying vital features of a microstructure that play important roles in the material behaviour. With a focus on developing multi-scale models for deformation and failure, this study is aimed at characterizing relevant microstructural features that affect this behaviour. An important task in this endeavour is to devise parameters that can quantify the size or shape of each heterogeneity Ξ_c^i and their spatial distribution in Ω_{mic}. Experimental and numerical studies in the literature [1, 2, 51, 52] have identified microstructural features that have major effects on damage in multi-phase microstructures. For instance, damage in cast A356 occurs by a combination of particle cracking in Ξ_c^i, microcrack formation and growth in the matrix Ξ_m and coalescence of the microcracks in Ω_{mic}. Particle cracking depends on size, aspect ratio and the extent of clustering. Bigger inclusions with high aspect ratio or those within a cluster show a higher propensity towards cracking. Various descriptors and functions used in the microstructural characterization process are discussed next.

4.1. Size descriptors

Size descriptors in terms of area, perimeter and longest diameter can be evaluated from the $I^b(x, y)$ data on heterogeneities in the binarized microstructure image of Ω_{mic}. Some of these metrics are defined below.

1. *Heterogeneity area* (A^i): is measured in terms of the total number of pixels belonging to an inclusion i in the binary digital image, defined as

$$A^i = \int_{\Xi_c^i} I_i^b(x, y)\, \mathrm{d}x\, \mathrm{d}y \tag{17}$$

   A more effective parameter is the local area fraction defined as $A_f^i = A^i / A_{\Omega_{\text{mic}}}$
2. *Perimeter* (P^i): is measured by the number of pixel-edges of the inclusion Ξ_c^i that interface with the matrix Ξ^m in a digital microstructure.
3. *Longest dimension* $(d_{\max}^i)$: is measured as the distance between two farthest points in the heterogeneity. It is useful in identifying the aspect ratio and defined as

$$d_{\max}^i = \text{Max}\{|\bar{r}_{AB}| \ \forall A(x_a, y_a), B(x_b, y_b) \in \Xi_c^i\} \tag{18}$$

DOI: 10.1002/nme

4.2. Shape descriptors

Shape descriptors quantify the shape and surface irregularities of heterogeneities and many are prescribed in the literature [50, 53]. Circularity and surface irregularities are important shape metrics that quantify reinforced microstructures like cast A356, and are represented by the following parameters:

1. *Roundness* (ρ^i): indicates how close the heterogeneity is to a circle and is effective for images of arbitrary shape, for which aspect ratio is not well defined. For the ith heterogeneity, it is defined as [50]

$$\rho^i = \frac{4A^i}{\pi(d^i_{\max})^2} \tag{19}$$

   ρ^i varies from 1 for circular shapes to 0 for highly elongated shapes.
2. *Edge smoothness* (χ^i): describes surface irregularities, e.g. sharp corners, even if it has an overall high roundness. Form factor is defined in Reference [50] to delineate surface irregularities as

$$ff^i = \frac{4\pi A^i}{(P^i)^2} \tag{20}$$

   The form factor is sensitive to surface irregularities, having a unit value for smooth surfaces and approaching zero for rough surfaces. It is also affected by the aspect ratio. The roundness and form-factor of various sample particles of Figure 15 are shown in Table I. Though ff^i for particles 8–11 captures the visible surface irregularities, it is very low for particles 4–7, which have smooth surfaces. A new parameter called edge smoothness is consequently

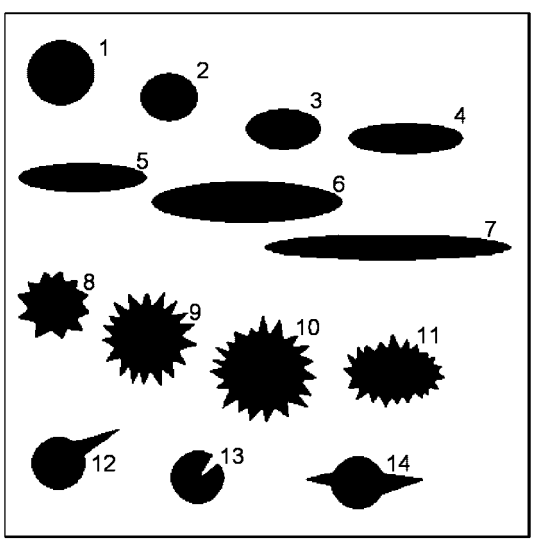

Figure 15. Image with simulated heterogeneities for testing the shape description parameters.

DOI: 10.1002/nme

Table I. Various size and shape description parameters for an image with simulated heterogeneities in Figure 15.

Heterogeneity no.	% Area frac. (A_f)	Roundness (ρ)	Form factor (ff)	Edge smooth. (χ)
1	1.25	0.9698	0.9909	0.6928
2	0.79	0.8431	0.8631	0.7069
3	0.87	0.5540	0.5559	0.7436
4	1.04	0.2776	0.2776	0.7115
5	1.08	0.2324	0.2325	0.6880
6	2.27	0.2179	0.2179	0.6796
7	1.87	0.1056	0.1073	0.5512
8	1.12	0.6848	0.7317	0.4318
9	1.89	0.6857	0.7193	0.2453
10	2.37	0.6605	0.7094	0.2675
11	1.58	0.5223	0.5495	0.3337
12	0.96	0.3471	0.3655	0.5806
13	0.75	0.9195	0.9274	0.4947
14	1.05	0.2508	0.2694	0.5749

introduced to capture the surface irregularities without being influenced by the aspect ratio. It is defined as

$$\chi^i = \sqrt{ff^i \times \frac{\pi d^i_{\max}}{(P^i)}} = \sqrt{\frac{4\pi^2 A^i d^i_{\max}}{(P^i)^3}} \tag{21}$$

In this parameter, the form factor is amplified by the effect of the largest dimension in the heterogeneity for better representation of surface irregularities. Also, the square root helps in depicting a better separation between different geometries, since the parameter is generally less than 1. χ closer to 0 indicates a large number of surface irregularities. However with pixel representation of boundaries in a digital image, χ can be closer to unity even for a perfect circle.

4.3. Spatial distribution descriptors

Characterization of spatial distribution quantifies the relative location of heterogeneities Ξ^i_e in the matrix Ξ_m. Spatial analysis can reveal characteristics of important material properties like isotropy, homogeneity, periodicity or clustering. Quantification of spatial distribution using Voronoi tessellation techniques has been introduced for heterogeneous materials in References [37, 54–57] for determining cumulative distribution function, probability density function, second-order intensity function or pair distribution function, distributions for nearest-neighbour distances, local area fractions, etc. Image-based characterization has been conducted in Reference [58] using the commercial package *Micromorph* in Reference [59] for evaluating mean free path, nearest neighbour distance and in Reference [60] for detecting clusters using spatial statistics. While most of these descriptors quantify nearest neighbour distance in microstructures of regular shaped inclusions, similar properties are not well established for arbitrary microstructural morphologies. Also, while a few descriptors have implicit reference to clustering, there is no metric that can quantify clustering in a definite manner. A morphological tool, viz. the covariance function [61] is implemented in this

DOI: 10.1002/nme

paper to evaluate the nearest neighbour distance, isotropy and periodicity. Also explicit descriptors are introduced to quantify clustering.

4.3.1. Covariance function. Covariance is a morphological function that can be applied to a digital image $I^b(x, y)$, $\forall x, y \in R^2$, for quantifying intricate spatial features of a heterogeneous microstructure. The covariance function $K(h)$ is defined in Reference [61] as the Lebesgue measure of a deterministic compact set $\mathbf{X}$ in $\mathbf{R}^n$, that is eroded by $\mathbf{B} = \{0, h\}$, which is a set of points at the ends of a vector $\mathbf{OH}$. For digital images of multiphase microstructures, $\mathbf{X}$ corresponds to the set of all the points that belong to the heterogeneities and $\mathbf{B}$ is a structural element consisting of two end pixels separated by a distance h and making an angle (α) with the reference axis. For $\alpha = 0°$ and $\alpha = 90°$ in the binary digital images, the function can be expressed as

$$\begin{aligned} K(h)_{(\alpha=0°)} &= \mathrm{Mes}(\mathbf{X} \ominus \mathbf{B}) = \int_{\mathbf{R}^n} I^b(x, y) \cdot I^b(x + h, y)\, \mathrm{d}x\, \mathrm{d}y \\ K(h)_{(\alpha=90°)} &= \int_{\mathbf{R}^n} I^b(x, y) \cdot I^b(x, y + h)\, \mathrm{d}x\, \mathrm{d}y \end{aligned} \tag{22}$$

where $I^b(x, y)$ (see Equation (16)) is the binary indicator function of the image associated with the set $\mathbf{X}$, and $\mathbf{X} \ominus \mathbf{B}$ indicates the erosion of set $\mathbf{X}$ by the element $\mathbf{B}$. The set $\mathbf{X}$ in the binarized microstructure is defined as

$$\mathbf{X} = \sum_{i=1}^{N_c} \Xi_c^i = \Omega_{\mathrm{mic}} - \Xi_m \tag{23}$$

The eroded set $\mathbf{X} \ominus \mathbf{B}$ may be expressed as $\mathbf{X} \cap \mathbf{X}_h$, where $\mathbf{X}_h$ is a translated set of $\mathbf{X}$. For any point x

$$x \in (\mathbf{X} \ominus \mathbf{B}) \quad \text{iff } x, x + h \in \mathbf{X} \tag{24}$$

For $I^b(x, y) = 1$, $K(h)$ denotes the total number of events for which pixel points (x, y) and $(x + h, y)$ both belong to the inclusion region. Computationally, it is evaluated as the number of inclusion pixels that overlap when the image is translated by a distance h at an angle α to the reference direction, and overlaid on itself. The covariance function for the micrograph 12(c) of the A356 alloy is plotted in Figure 16(a) for $\alpha = 0°$ and $\alpha = 90°$. $K(h)$ in these plots is normalized with the total number of pixels in the image. The plots capture the average properties at shorter translations ($\leqslant h$) as well as the behaviour of the spatial distribution at larger translations. Important features that can be captured by the covariance function are discussed below.

1. *Average nearest neighbour distance* (l_{nnd}): For smaller values of h, $K(h)$ corresponds to the intersection of an inclusion with its own translated image. Consequently it decreases rapidly with h with decreasing self overlay. The small increase in $K(h)$ at higher values of h refers to the intersection with neighbours. Hence, the average nearest neighbour distance of a micrograph corresponds to the smallest value of h at which $K(h)$ is a local minimum. The first local minima of $K(h)$ in Figure 16(a) occur at 4 μm for $\alpha = 0°$ and 4.5 μm for $\alpha = 90°$. These correspond to the average nearest neighbour distance in the two orthogonal directions. $K(h)$ is also able to qualitatively indicate the presence of a cluster, since the first minimum should approach a zero value in the absence of clusters. To illustrate the effectiveness of $K(h)$ in identifying clusters, two microstructures containing elliptical inclusions are simulated. As

DOI: 10.1002/nme

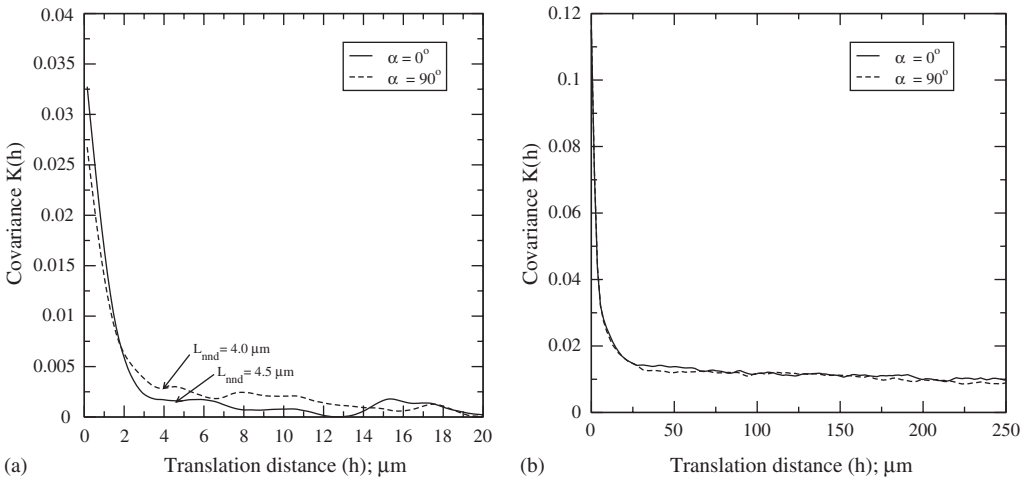

Figure 16. Covariance ($k(h)$) plots of the A356 microstructure: (a) $K(h)$ for micrograph in Figure 12(c); and (b) $K(h)$ for micrograph in Figure 2.

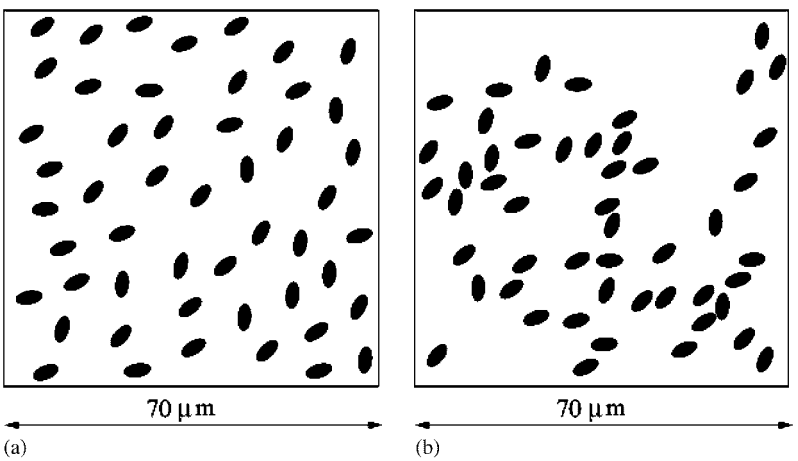

Figure 17. Simulated microstructures containing 50 inclusions with: (a) low clustering (A); and (b) high clustering (B).

shown in Figures 17(a) and (b), they represent low and high clustering levels, respectively. The $K(h)$ plots in Figure 18 show that the first local minimum for the sparse distribution reaches a value close to zero, while clustered microstructure has a non-zero minimum of 0.008.

2. *Periodicity and isotropy*: The covariance plot in Figure 18 of the simulated microstructure 17(a) shows a rise to a local maxima following the first minima. This behaviour can be observed multiple times for some micrographs, leading to an oscillatory behaviour of $K(h)$. This phenomenon has been termed as the pseudo-periodic effect in Reference [61]. While periodic covariance is generally an outcome of a periodic process, an aperiodic structure

DOI: 10.1002/nme

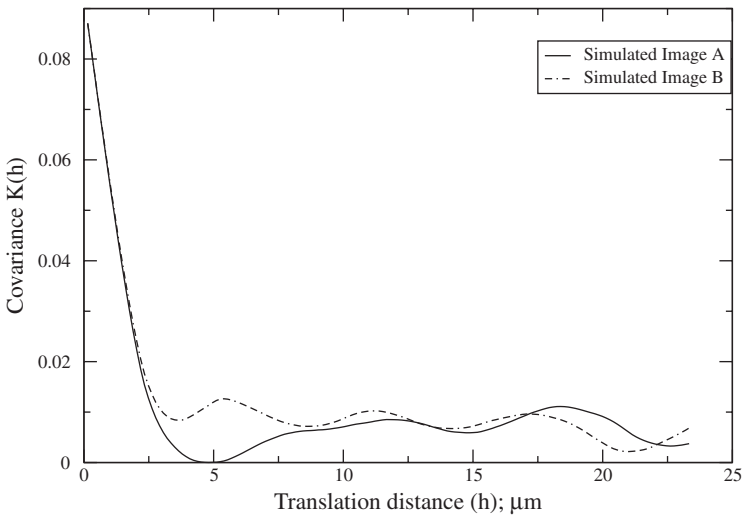

Figure 18. Covariance of simulated microstructures *A* and *B* of Figure 17.

under some circumstances can also give a periodic covariance, as discussed in Reference [61]. Hence, other metrics are also necessary to confirm periodicity.

Isotropy can be estimated by comparing the covariance function plots in two orthogonal directions for directionality. The covariance plots for the micrograph window 12(c) in Figure 16(a) shows that the $K(h)$ values are not equal in the two directions. However, when the covariance of the larger parent micrograph of Figure 2 is plotted in Figure 16(b), an isotropic behaviour is observed.

4.3.2. Cluster index. Clustering in spatial distributions is manifested by a high local density of second phase heterogeneities. In the A356 micrograph of Figure 2, large regions of Al matrix are surrounded by clusters of Si particles that act as local stress risers. This structure is formed by solidification, where the growing aluminium dendrites force the Si particles into spaces between the dendrite arms. This results in clustering of silicon particles around the secondary dendrite arms. A method of quantifying the dendrite arm size is the secondary dendrite arm spacing (SDAS), which is measured as the average centre to centre distance of the secondary dendrite arms. However, SDAS does not give specific information about local clustering. For a better quantification of local clustering, two metrics, viz. *spacing index* (SI) and *clustering intensity* (CI) are implemented. These metrics quantify the number of inclusions concentrated in a particular region and the size of the matrix that is free of inclusions, respectively. The parameters are normalized with respect to a characteristic radius R_{ch} that is defined as

$$R_{\text{ch}} = \sqrt{\frac{A_{\text{image}}}{\pi N}} \tag{25}$$

where A_{image} is the image area and N is the total number of inclusions. R_{ch} signifies the inter-particle distance for an ideal distribution of circular particles in the image. The spacing index (SI) is a measure of the dendrite arm size, which is estimated as the radius of the biggest circle that can

DOI: 10.1002/nme

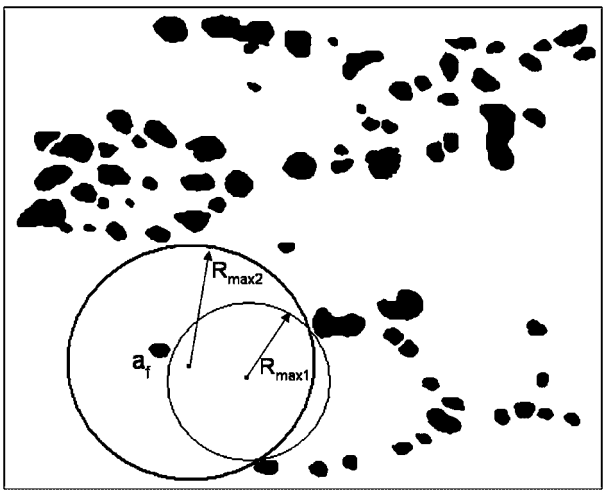

Figure 19. Microstructure showing regions that have pockets of few inclusions in large matrix regions.

fit into the micrograph without intersecting any particles normalized by R_{ch}. However, as shown in Figure 19, tiny stray particles in the matrix region can result in lower than reasonable values of the arm size. To prevent this error, the spacing radius is evaluated beyond the first interfering particle to check if the radius increases drastically (at least 25%). In that event, a new radius is used with a compensating multiplication factor for the particles engulfed, i.e.

$$\text{SI} = \frac{R_{\max}(1 - a_f)}{R_{\text{ch}}} \tag{26}$$

where a_f is the area fraction of the interfering particle.

Cluster intensity (CI), on the other hand, measures the intensity of packing in a cluster. Karnezis [59] has evaluated CI by a quadrant method, where the image is divided into finite squares and clustering is identified by the number of particles inside each square. A shortcoming with this method is that it cannot detect clusters across boundaries of already fixed quadrants. To overcome this, the cluster intensity CI is restated as the normalized difference between the maximum and minimum number of particles enclosed within a characteristic circle of radius R_{ch}, i.e.

$$\text{CI} = \frac{N^e_{\max}(x_{\max}, y_{\max}) - N^e_{\min}(x_{\min}, y_{\min})}{N^e_{\text{avg}}} \tag{27}$$

where $N^e_{\max}$ and $N^e_{\min}$ are the maximum and minimum number of heterogeneities inside the characteristic circle at points $(x_{\max}, y_{\max})$ and $(x_{\min}, y_{\min})$ of the microstructure, respectively and N_{avg} is the average number of heterogeneities inside the characteristic circle over the entire microstructure. A new parameter called cluster index ($\kappa = \text{SI} \times \text{CI}$) is introduced for quantifying clustering in the microstructure. The values of the cluster index for the simulated images of Figures 17(a) and (b) are $\kappa = 4.30$ and $\kappa = 6.91$, respectively. This establishes the effectiveness of the cluster index as a metric for identifying clusters.

DOI: 10.1002/nme

4.3.3. Cluster contour. Contour plots of parameters representing the spatial distribution are also helpful in identifying clusters. Such a contour plot can be generated using the characteristic radius R_{ch} as the field of influence of each heterogeneity. The total area of heterogeneities inside of each characteristic circle is measured as contour intensity (COIN) at a point. The cluster contour index is then defined in terms of the contour intensity as

$$\iota = 1 - \frac{\text{COIN}_{\text{mean}}}{\text{COIN}_{\text{maximum}}} \tag{28}$$

The mean and maximum values of COIN are evaluated from all points in the micrograph. A contour index $\iota = 1.0$ denotes high clustering, while values closer to zero indicate uniform distribution. The contour index accounts for the area fraction of inclusions within a prescribed region while the cluster index considers the number of inclusions in this region. The cluster contours of the simulated images 17(a) and (b) are plotted in Figures 20(a) and (b), for which the contour index values are $\iota = 0.551$ and $\iota = 0.723$, respectively. In Table II, various characteristic functions of size, shape and spatial distributions are documented for the WIGE algorithm simulated micrograph of Figure 13(b), and the corresponding SEM micrograph of Figure 12(b). The excellent

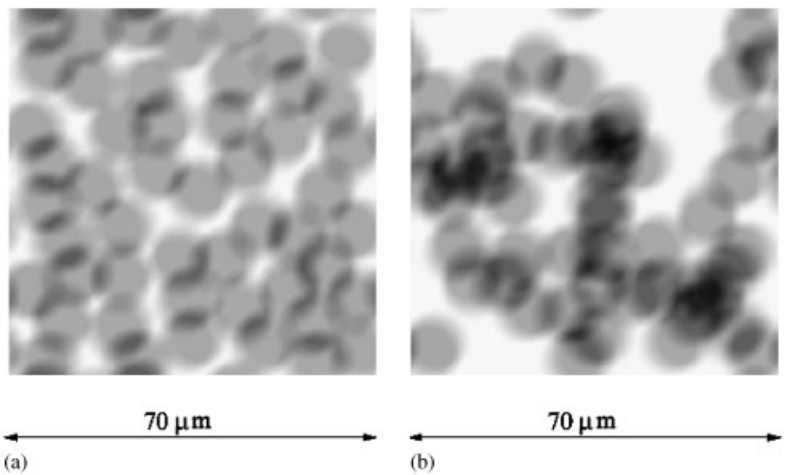

Figure 20. Cluster contour of simulated micrographs *A* and *B* in Figures 17(a) and (b), respectively.

Table II. Microstructural characteristic functions of a high resolution SEM micrograph of Figure 12(b) and a corresponding WIGE algorithm simulated micrograph of Figure 13(b).

Parameter	SEM micrograph	Simulated micrograph
No. of inclusions	75	72
Area fraction A_f	4.52%	4.50%
Least roundness ρ	0.37	0.35
Least edge smoothness χ	0.55	0.52
Cluster index κ	20.41	19.77
Contour index ι	0.84	0.83

DOI: 10.1002/nme

agreement in the values of characteristic functions validates the effectiveness of the WIGE algorithm.

The size, shape and spatial distribution descriptors quantify microstructural characteristics that can be used for determining the scale of different regions of a computational domain in a multiscale modelling framework. The following section addresses a method to delineate this multi-scale morphology based domain partitioning (MDP) as a precursor to multiscale modelling.

5. MORPHOLOGY BASED DOMAIN PARTITIONING (MDP) AS A PREPROCESSOR FOR MULTISCALE MODELLING

The concurrent multi-level models of Figure 1, that have been developed in References [16–18, 28] for multi-scale modelling of heterogeneous materials, inherently undergo domain partitioning based on the evolution of stresses, strains and/or damage in the microstructure. An assumption is made in the previous work that the entire computational domain is initially homogenizable for purely macroscopic computations. Concurrent micro-regions emerge in the computational domain with evolving deformation and other variables in the microstructure. However, many heterogeneous materials such as the cast aluminium alloy A356 considered in this study have natural multiple length scales even from a morphological point of view. A low resolution micro-region of this material is shown in Figure 21. The geometric features of the local morphology render some regions statistically inhomogenizable, i.e. statistically equivalent representative volume elements or SERVEs cannot be identified for these regions due to high local gradients in geometric features. Detailed description of statistical homogeneity and methods of identifying a SERVE have been provided in Reference [62]. Hence, in a true concurrent multi-scale computational model, these regions of geometric inhomogeneity should be identified *a priori*, and modelled separately at

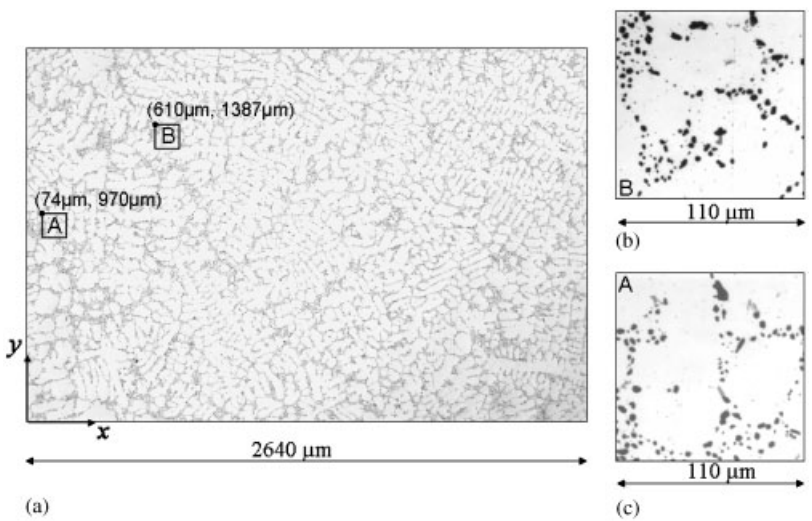

Figure 21. (a) A low resolution microstructural image of the cast aluminium alloy A356 macroscale considered for partitioning; and (b) and (c) high resolution micrographs for simulating high resolution images.

DOI: 10.1002/nme

different length scales in a concurrent setting. The resulting computational domain is expressed as $\Omega_{\text{comp}} = (\bigcup_{i=1}^{N_{\text{mac}}} \Omega^i_{\text{mac}}) \cup (\bigcup_{i=1}^{N_{\text{mic}}} \Omega^i_{\text{mic}})$, where the subscripts mac and mic correspond to regions that can and cannot be homogenized, respectively.

Once the high resolution microstructural features have been generated for all locations in the computational domain by the PIGE or WIGE algorithms described in Section 2, the microstructural characterization functions and tools described in Section 4 can be used for delineating regions with different scales in the multi-scale model. The objective of this section is to develop criteria that can enable this partitioning of the computational domain into regions of homogeneity and inhomogeneity. Functions of the microstructural descriptors of Section 4 are developed for the underlying high resolution microstructure to establish the partitioning criteria. Successive domain partitioning and refinement are executed based on these criteria. The adaptive domain partitioning is limited by a homogeneous length scale parameter that separates statistically homogeneous regions from heterogeneous regions. This is discussed next.

5.1. Statistical homogeneity and homogeneous length scale (HLS)

A heterogeneous medium is defined as spatially stationary or statistically homogeneous, if the joint probability distributions describing the stochasticity of the microstructure is invariant with respect to translations [32]. For statistically homogeneous media, the n-point probability function S_n has been shown in Reference [32] to satisfy the condition

$$S_n(x_1, x_2, \ldots, x_n) = S_n(x_1 + y, x_2 + y, \ldots, x_n + y) = S_n(x_{12}, \ldots, x_{1n}) \quad \forall n \geqslant 1 \tag{29}$$

where $x_1, x_2, \ldots, x_n$ are position vectors of n points in the medium and $x_{ij} = x_j - x_i$. For a statistically homogeneous medium, S_n depends on the relative positions, rather than on the absolute positions. For this case, S_1 (the volume or area fraction) is a constant everywhere. Hence homogeneity in material microstructure can be assumed at regions, where S_1 does not vary significantly with location. This is the basis of establishing the homogeneous length scale in the material microstructure in Reference [63]. HLS is defined in Reference [63] as the dimension of the domain or the length scale above which the local variability in area fraction is smaller than a specified tolerance. The process of determination of HLS is as follows:

1. Consider a suitably large, high resolution, microstructure domain of characteristic dimension L.
2. The microstructure is divided into finite squares, each of size D.
3. The area fraction A_f of the heterogeneities in each square is evaluated. The ratio of standard deviation (σ_{A_f}) to the mean area fraction (μ_{A_f}) is defined as the coefficient of variation or COV, which denotes the variation in A_f between the squares.
4. The steps 2 and 3 are repeated for squares in the quilt of different sizes and the COV is evaluated for each square size.

For a Poisson distribution, the relation between the coefficient of variation and the normalized square size has been derived in Reference [63] as

$$\text{COV}(A_f) = \frac{\sigma_{A_f}}{\mu_{A_f}} = \left(\frac{\pi}{4A_f}\right)^{0.5} \left(\frac{D}{L}\right)^{-1} \tag{30}$$

The coefficient of variation in Equation (30), representing the variation of area fraction, varies linearly with the normalized quilt size in a logarithmic scale. Relation (30) suggests plotting

DOI: 10.1002/nme

the COV for squares of various sizes as a function of the normalized square size (D/L) on a logarithmic scale. A tolerance value is set for the COV for determining the (D/L) intercept from this plot. The homogeneous length scale HLS is consequently identified as the square size D. The tolerance value is important in the determination of HLS. This length scale is a threshold, below which it is necessary to change from a homogenized to a heterogeneous domain representation with explicit delineation of heterogeneities.

5.2. *Multiscale domain partitioning criteria*

The MDP operation requires: (i) high resolution microstructure representation, with respect to key characteristic features, in the entire computational domain Ω_{comp}, (ii) the homogeneous length scale HLS, and (iii) representative functions of key microstructural descriptors. Since extreme values of the microstructural morphology play important roles in the localization and failure behaviour of heterogeneous materials, descriptors that reflect these characteristics are considered important in this study. The method begins with a coarse discretization of Ω_{comp} into N_p^0 subdomains or partitions, as shown in Figure 23(a). A microstructural unit is defined as a high resolution microstructural region Ω_{mic} of dimension $\xi * \text{HLS}$ where $\xi < 1$. In this study, the factor is chosen as $\xi = 0.5$. Each subdomain i is assumed to be made up of M^i underlying microstructural units. For successive partitioning of a subdomain i due to lack of homogeneity, statistical functions representing the variation of a descriptor in the M^i microstructural units are evaluated.

Size and shape descriptors in the refinement criteria include area fraction (A_f), roundness (ρ) and edge smoothness (χ), while the spatial distribution descriptors include cluster index (κ), contour index (ι) and the nearest neighbour distance (L_{nnd}). Four functions of these descriptors are introduced to quantify their statistical variation. The selection of these functions is non-unique and somewhat *ad hoc*, but they provide a useful example.

1. $\mathbf{F}^1$: This function is a coupled representation of the area fraction (A_f) and cluster index (κ). High values of both these descriptors are detrimental to the material failure response. Consequently, the function is constructed in terms of the mean (μ) of the descriptors and is expressed as

$$\mathbf{F}_i^1 = \mu(A_f)\mu(\kappa) \tag{31}$$

   The parameters $\mu(A_f)$ and $\mu(\kappa)$ are evaluated for the M^i microstructural units within each subdomain i. $\mathbf{F}^1$ is more appropriate for cases where the size variation of heterogeneities is not significant.
2. $\mathbf{F}^2$: This function is a variant of $\mathbf{F}^1$, in which the cluster index (κ) is replaced by the contour index (ι) and is expressed as

$$\mathbf{F}_i^2 = \mu(A_f)\mu(\iota) \tag{32}$$

   $\mathbf{F}^2$ is relevant when the area of the heterogeneities, evaluated in ι, is important for identifying clusters. It can accommodate considerable variation in the size of heterogeneities.
3. $\mathbf{F}^3$: This function utilizes the spatial distribution of the heterogeneity nearest neighbour distance (L_{nnd}) as a measure of clustering. Lower values of L_{nnd} indicate higher degree of clustering (inverse correlation). Consequently an alternative form, which has a direct

DOI: 10.1002/nme

correspondence to the degree of clustering, is written as

$$\hat{L}_{\text{nnd}} = 1 - \frac{L_{\text{nnd}}}{L_{\Omega_{\text{mic}}}}$$

where $L_{\Omega_{\text{mic}}}$ is the length of entire local microstructure Ω_{mic}. The resulting refinement function is then written as the mean of the product $A_F \hat{L}_{\text{nnd}}$ as shown below

$$\mathbf{F}_i^3 = \mu(A_f \hat{L}_{\text{nnd}}) \tag{33}$$

This function does not accommodate size and shape variations and is effective for microstructures with minimal variation in shape features.

4. $\mathbf{F}^4$: When both the shape and size of heterogeneities are important in microstructural characterization, a function combining shape and size parameters may be defined as

$$S_e = 1 + \sum_{k=1}^{N_c} \left[\frac{A_f^k}{A_f} (w_\rho (1 - \rho_k) + w_\chi (1 - \chi_k)) \right] \tag{34}$$

where A_f^k and A_f are the local area fraction of the kth heterogeneity and the overall area fraction for the subdomain Ω_{mic}, respectively, and ρ_k and χ_k are the roundness and edge smoothness of the kth heterogeneity, respectively. N_c is the number of heterogeneities in Ω_{mic} and w_ρ, w_χ are weights that are assigned to the two shape descriptors. The weights in this study are taken as $w_\rho = 0.5$, $w_\chi = 0.5$. The term $(1 - \rho)$ is high for higher aspect ratios, while $(1 - \chi)$ increases with increasing surface irregularities. The normalized local area fraction A_f^k in the product gives a higher weight to heterogeneities of larger size, for which shape effects dominate. It should be noted that for microstructures where the aspect ratio or roughness are not pronounced, the value of S_e tends to 1.0. The contour index (ι) and the overall area fraction A_f are multiplied with S_e in the refinement function to capture spatial density of heterogeneities as well. The resulting function is written as

$$\mathbf{F}_i^4 = \mu(S_e \cdot A_f \cdot \iota) \tag{35}$$

Statistical homogeneity is assumed for a subdomain in the microstructure if the values of the functions described above do not change considerably for any sub-region of that domain. Thus, starting from the initial computational domain, successive subdomain partitioning is performed based on criteria in terms of these functions. Only four partitions of each subdomain are considered in each refinement stage as shown in Figure 23(b). The four refinement functions $\mathbf{F}_i^1$, $\mathbf{F}_i^2$, $\mathbf{F}_i^3$ and $\mathbf{F}_i^4$ are evaluated in each subdomain together with each of its four partitions $\mathbf{F}_i^k(l)$, $(l = 1, \ldots, 4)$. A subdomain (i) is partitioned only if the following criterion holds for any of the four sub-regions:

$$\frac{|\mathbf{F}_i^k - \mathbf{F}_i^k(l)|}{\mathbf{F}_i^k} > C_{f1} \quad \text{for any } l = 1, \ldots, 4 \tag{36}$$

where C_{f1} is a prescribed tolerance. The tolerance should be chosen judiciously, such that only the critical domains are partitioned. A value of $C_{f1} = 0.15$, corresponding to 15% variation is chosen in this paper. This value may be better determined from micromechanical analyses.

DOI: 10.1002/nme

The refinement process locally reduces the subdomain size and ultimately can go below the dimension of the homogeneity limit or HLS. Once a subdomain reaches the HLS dimension through successive local partitioning, only one level of further partitioning is possible. The level below HLS is not homogenizable and hence cannot be refined any further. A special criterion is required for partitioning once the threshold dimension HLS is reached. Each of the subsequent partitions contain only one microstructural unit (M^{loc}) of dimension $0.5 * \text{HLS}$. It is not possible to evaluate the statistical functions $\mathbf{F}^k$, $k = 1, \ldots, 4$ for a single (M^{loc}). The criterion is constructed in terms of the variation of average local area fraction A_f, an important descriptor that is present in all the refinement functions $\mathbf{F}^k$. Partitioning below HLS is governed by the equation

$$\frac{|(A_f)_i - (A_f)_i(l)|}{(A_f)_i} > C_{f2} \quad \text{for } l = 1, \ldots, 4 \tag{37}$$

Any sub-domain below the HLS threshold is characterized by significant variation in microstructural characterization functions, e.g. the local area fraction. Consequently those partitions for which the variation is really large are classified as inhomogeneous and opened up for explicit microstructural representation in the multi-level model of Figure 1. The factor C_{f2} is taken as 0.75, corresponding to a 75% difference, to capture critical regions in the microstructure. The combined microstructure *simulation–characterization–partitioning* method helps delineate and layout the hierarchy of scales in the computational model.

6. A NUMERICAL EXAMPLE

The domain partitioning algorithm is applied to the cast aluminium alloy A356 microstructure for demonstrating its effectiveness. The low resolution computational domain Ω_{comp} of dimensions 2640 μm × 1760 μm is shown in Figure 21. The PIGE algorithm of Section 2.1 is implemented to generate high resolution images of all points in Ω_{comp}. The correlation table in Figure 6 is constructed with two 110 μm × 110 μm high resolution images at locations **A** (74 μm, 970 μm) and **B** (610 μm, 1387 μm) as shown in Figures 21(b) and (c). The spatial distance based weighting of Equation (9) is applied to create a sequence of contiguous high resolution microstructural images. Size, shape and spatial descriptors, discussed in Section 4, are evaluated for each of the simulated high resolution microstructural images. Next, the homogeneous length scale HLS delineating the threshold of homogeneous length scale is evaluated using the procedure outlined in Section 5.1. The $\text{COV} - D/L$ plot for identifying HLS is shown in Figure 22, where the reference dimension is taken as $L = 1760$ μm. The HLS data is obtained for domains of two different sizes, viz. 1760 μm × 1760 μm and 880 μm × 880 μm. Figure 22 shows that the HLS plot is not much affected by the choice of the domain size and location. The HLS is obtained as 110 μm with a tolerance value in the area fraction COV of 0.2.

The computational domain shown in Figure 21(a) is initially divided into 6 subdomains to start the partitioning process. Successive partitioning progresses according to the refinement criteria in Section 5, till the subdomain size reaches below the HLS. Three cycles of successive refinement are conducted till the HLS is reached. The corresponding functions $|\mathbf{F}_i^k - \mathbf{F}_i^k(l)|/\mathbf{F}_i^k$, $k = 1, \ldots, 4$ values in Equation (36) are reported in Tables III, IV and V. In Table III, the highest values of the functions are listed for the first cycle of domain partitioning. The subdomains of this table are marked in Figure 23(a). The functions have similar values for the descriptors $\mathbf{F}_i^2$, $\mathbf{F}_i^3$ and $\mathbf{F}_i^4$ and hence all of them point to the partitioning of the same subdomain 4 of Figure 23(a). The resulting

DOI: 10.1002/nme

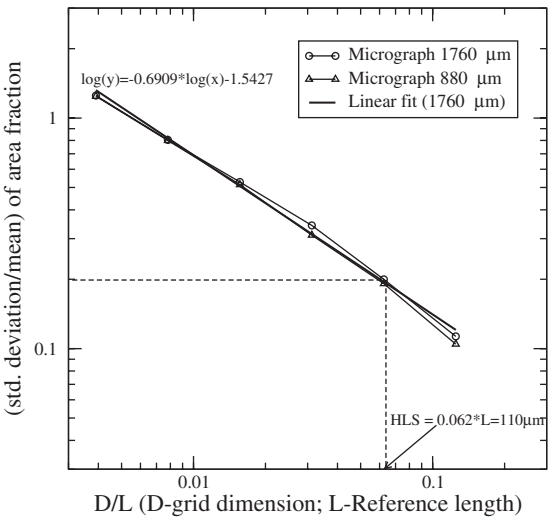

Figure 22. Determination of the homogeneous length scale HLS for A356 microstructure with micrographs of two different dimensions. The figure shows a linear fit in the log scale.

Table III. Highest values of the functions $|\mathbf{F}_i^k - \mathbf{F}_i^k(l)|/\mathbf{F}_i^k$, $k = 1, \ldots, 4$ values in Equation (36) for the first cycle of domain partitioning in subdomains 1–6 shown in Figure 23(a).

Subdomain no. (i)	$k=1$	$k=2$	$k=3$	$k=4$
1	0.1429	0.1209	0.1231	0.1069
2	0.1628	0.0669	0.0798	0.0709
3	0.0885	0.0845	0.0841	0.0902
4	0.1454	0.1964	0.2162	0.1937
5	0.0888	0.0115	0.0387	0.0224
6	0.1637	0.0732	0.0792	0.0758

Table IV. Highest values of the functions $|\mathbf{F}_i^k - \mathbf{F}_i^k(l)|/\mathbf{F}_i^k$, $k = 1, \ldots, 4$ for the second cycle of domain partitioning in subdomains 1–4 shown in Figure 23(b).

Subdomain no. (i)	$k=2$	$k=3$	$k=4$
1	0.2299	0.2471	0.2110
2	0.1876	0.1977	0.1755
3	0.1225	0.1247	0.1272
4	0.0450	0.0434	0.0397

partitioning is shown in Figure 23(b). For $\mathbf{F}_i^1$, the function has a value 0.1454 in subdomain 4, which is marginally below the criterion value 0.15 and hence is not selected for refinement. This results in a different refinement from the other three functions. Consequently, only $\mathbf{F}_i^2$, $\mathbf{F}_i^3$ and $\mathbf{F}_i^4$ are retained for the subsequent partitioning cycles shown in Figures 23(b), (c) and (d). For

DOI: 10.1002/nme

Table V. Highest values of the functions $|\mathbf{F}_i^k - \mathbf{F}_i^k(l)|/\mathbf{F}_i^k$, $k = 1, \ldots, 4$ for the third cycle of domain partitioning in subdomains 1–8 shown in Figure 23(c).

Subdomain no. (i)	$k=2$	$k=3$	$k=4$
1	0.2502	0.2455	0.2466
2	0.2843	0.2901	0.3036
3	0.5002	0.4846	0.4183
4	0.1703	0.1824	0.1684
5	0.3972	0.4836	0.4220
6	0.1826	0.2011	0.1898
7	0.2839	0.3041	0.2816
8	0.0901	0.1010	0.1004

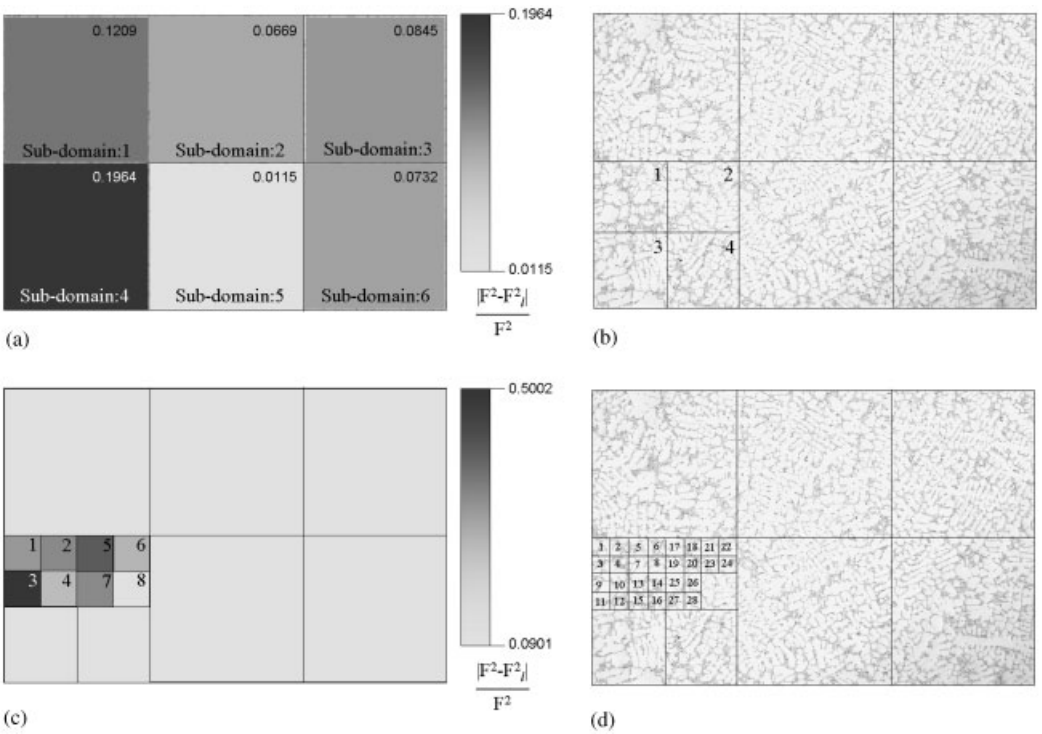

Figure 23. The domain partitioning process using Equations (36) and (37): (a) the distribution of the function $|\mathbf{F}^2 - \mathbf{F}^2_{(l)}|/F^2$ for the 6 subdomains; (b) the first cycle of domain partitioning into 4 smaller subdomains; (c) the distribution of the partitioning function for the second cycle refinement; and (d) result of third cycle of partitioning to yield the final hierarchical model.

each of these cycles, the highest value of $|\mathbf{F}_i^k - \mathbf{F}_i^k(l)|/F_i^k$, $k = 2, \ldots, 4$ in each subdomain is tabulated in Tables IV and V. The subdomain numbers are labelled in Figures 23(b) and (c), respectively. The figures show the contours of the function $|\mathbf{F}^2 - \mathbf{F}^2(l)|/F^2$. The partitioning process continues till the size limit of HLS = 110 μm is reached. At this stage, Equation (37) is

DOI: 10.1002/nme

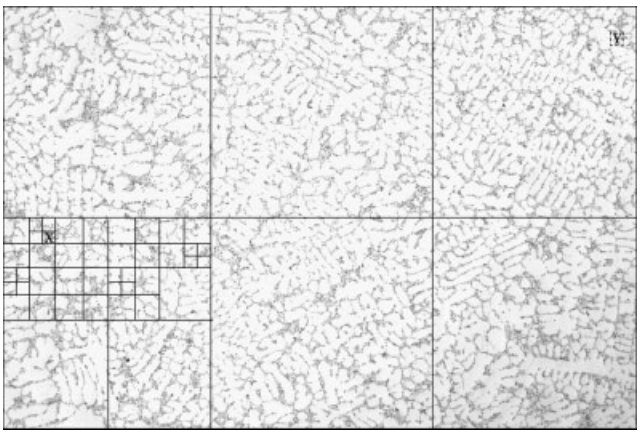

Figure 24. The final computational domain partitioned using Equation (36) with any of descriptors $\mathbf{F}^2$, $\mathbf{F}^3$ or $\mathbf{F}^4$ and Equation (37).

Table VI. Comparison of microstructural characteristics at a critical region **X** and a non-critical region **Y** shown in Figures 25(a), and (b) respectively.

Parameter	Micrograph **X**	Micrograph **Y**
No. of inclusions	38	15
Area fraction A_f	12.87%	3.78%
Least roundness ρ	0.24	0.35
Least edge smoothness χ	0.31	0.58
Cluster index κ	7.31	5.64
Contour index ι	0.82	0.79

used for the final refinement. The final partitioned computational domain is shown in Figure 24. The hierarchy of partitioned domains, shown in Figure 24, does not change with any of these functions in the criterion. Partitioning with $\mathbf{F}^1$ leads to a much higher number of subdomains that renders it computationally expensive.

To verify the effectiveness of the partitioning method in identifying critical regions, the microstructure in a sub-HLS region is compared with a region that has not been partitioned by the algorithm. The window **X** marked in Figure 24 corresponds to a region that has been achieved through the maximum successive partitioning. In contrast, the window **Y** is from a region that has been untouched by the refinement. Simulated binary images of high resolution micrographs at these two locations are shown in Figures 25(a) and (b), respectively. The simulated micrograph 25(a) with 38 clustered inclusions is more critical than 25(b) with approximately 15 similar sized inclusions. Characteristic functions of size, shape and spatial distribution are tabulated in Table VI for the two micrographs. All these functions indicate that the micrograph 25(a) at location **X** is more detrimental to the material response than micrograph 25(b) at location **Y** and hence the effectiveness of the overall approach is established.

DOI: 10.1002/nme

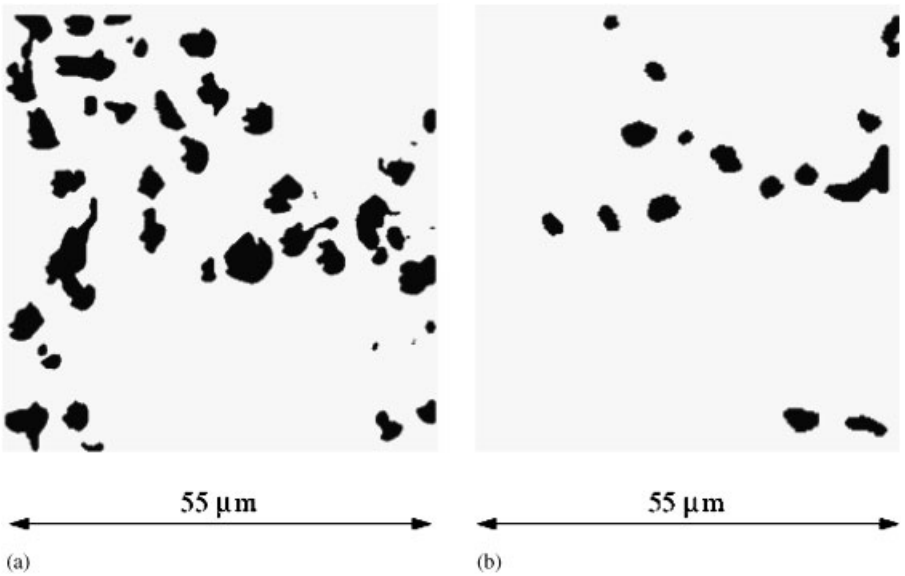

Figure 25. High resolution microstructural images of regions labelled in Figure 24: (a) critical region labelled **X**; and (b) non-critical region labelled **Y**.

7. CONCLUSIONS

This paper is intended as a comprehensive pre-processor to multi-scale simulation of mechanical behaviour and damage in heterogeneous multi-phase materials. Three sets of methods and algorithms are developed towards this goal. The methods are strictly based on geometric features of the material morphology and do not use any mechanical response functions. The first set comprises of methods for simulating high resolution microstructural images from low resolution optical or scanning electron micrographs and a limited set of high resolution micrographs. Experimental acquisition of a large set of contiguous micrographs for creating a montage of images in any material domain is a difficult exercise. Aside from the time and expenses incurred in the acquisition process itself, perfect alignment of the microscope for non-overlapping adjoining domains is a non-trivial task. The proposed set of computational algorithms can aid significantly in this acquisition-reconstruction process. Two methods, viz. the polynomial interpolation with greyscale based enhancement (PIGE) and the wavelet interpolation with greyscale based enhancement (WIGE) are proposed in this work. Excellent convergence characteristics are observed for both methods with respect to 1-point, 2-point and 3-point probability functions. For the material considered in this paper, the WIGE method is found to yield slightly better result than the PIGE method. While the methodology developed is validated for multi-phase cast aluminium alloys consisting of intermetallics and particles, it can be easily applied to fibre/particulate reinforced composites and extended for more complicated polycrystalline alloy systems.

The second set of methods consists of material characterization tools for quantifying the microstructural features. The tools invoke parametric descriptors of size, shape and spatial distributions of the heterogeneities. The effectiveness of these descriptors in identifying specific microstructural

DOI: 10.1002/nme

features that affect mechanical behaviour and failure is tested for a cast aluminium alloy A356 microstructure in this step.

The third and final set of methods are for multiscale morphology based domain partitioning (MDP) for delineating subdomains of different scales in a concurrent multi-scale analysis model. The first step in this objective is the estimate of a homogeneous length scale or HLS as a homogenization threshold. HLS helps in the delineation of statistically homogeneous and heterogeneous regions in a multi-phase material microstructure. Four descriptors are developed for incorporation in domain partitioning criteria. The descriptors are functions of microstructural parameters that are expected to affect material behaviour. Successive domain partitioning according to the criteria continues till the HLS is reached. A slightly different criterion is subsequently invoked to open regions where explicit representation of the multi-phase microstructure is necessary. The effectiveness of each of the descriptors and criteria in delineating multi-scale domain representations is demonstrated for a cast aluminium A356 microstructure. Follow on work on coupling the multi-scale domain partitioning with multi-scale analysis is currently underway and will be reported in a future paper.

ACKNOWLEDGEMENTS

This work has been supported by the National Science Foundation NSF Div Civil and Mechanical Systems Division through the GOALI Grant No. CMS-0308666 (Program director: Dr Jorn Larsen-Basse and Dr Y-W. Chung). This sponsorship is gratefully acknowledged. The authors are grateful to Drs Steve Harris and James Boileau of Ford Research Laboratory for providing materials specimens to be characterized and many discussions. Computer support by the Ohio Supercomputer Center through Grant PAS813-2 is also gratefully acknowledged.

REFERENCES

1. Wang QG, Caceres CH, Griffiths JR. Damage by eutectic particle cracking in Aluminum casting alloys A356/357. *Metallurgical and Materials Transactions A* 2003; **34**:2901–2912.
2. Wang QG. Microstructural effects on the tensile and fracture behavior of Aluminum casting alloys A356/357. *Metallurgical and Materials Transactions A* 2003; **34**:2887–2899.
3. Argon AS, Im J, Sofoglu R. Cavity formation from inclusions in ductile fracture. *Metallurgical and Materials Transactions A* 1975; **6**:825–837.
4. Christman T, Needleman T, Suresh S. An experimental and numerical study of deformation in metal-ceramic composites. *Acta Metallurgica et Materialia* 1989; **37**:3029–3050.
5. Gonzalez C, Llorca J. Prediction of the tensile stress–strain curve and ductility in Al/SiC composites. *Scripta Metallurgica* 1996; **35**(1):91–97.
6. Weissenbek E, Boehm HJ, Rammerstoffer FG. Micromechanical investigations of fiber arrangement effects in particle reinforced metal matrix composites. *Computational Materials Science* 1994; **3**:263–278.
7. Segurado J, Llorca J. A computational micromechanics study of the effects of interface decohesion on the mechanical behavior of composites. *Acta Materialia* 2005; **53**:4931–4942.
8. Boehm HJ, Han W, Ecksclager A. Multi-inclusion unit cell studies of reinforcement stresses and particle failure in discontinuously reinforced ductile matrix composites. *Computer Modeling in Engineering and Sciences* 2004; **5**:5–20.
9. Yang S, Gokhale AM, Shan Z. Utility of microstructure modeling for simulation of micro-mechanical response of composites containing non-uniformly distributed fibers. *Acta Materialia* 2000; **48**:2307–2322.
10. Shan Z, Gokhale AM. Digital image analysis and microstructure modeling tools for microstructure sensitive design of materials. *International Journal of Plasticity* 2004; **20**:1347–1370.
11. Terada K, Miura T, Kikuchi N. Digital image-based modeling applied to the homogenization analysis of composite materials. *Computational Mechanics* 1997; **20**(4):331–346.

DOI: 10.1002/nme

12. Ghosh S, Ling Y, Majumdar B, Kim R. Interfacial debonding analysis in multiple fiber reinforced composites. *Mechanics of Materials* 2000; **32**:561–591.
13. Li M, Ghosh S, Richmond O. An experimental-computational approach to the investigation of damage evolution in discontinuously reinforced aluminum matrix composites. *Acta Materialia* 1999; **47**(12):3515–3552.
14. Li S, Ghosh S. Extended Voronoi cell finite element model for multiple cohesive crack propagation in brittle materials. *International Journal for Numerical Methods in Engineering* 2006; **65**:1028–1067.
15. Smit RJM, Brekelmans WAM, Meijer HEH. Prediction of the mechanical behavior of nonlinear heterogeneous systems by multi-level finite element modeling. *Computer Methods in Applied Mechanics and Engineering* 1998; **155**(1–2):181–192.
16. Raghavan P, Ghosh S. Adaptive multi-scale computational modeling of composite materials. *Computer Modeling in Engineering and Sciences* 2004; **5**:151–170.
17. Ghosh S, Lee K, Raghavan P. A multi-level computational model for multi-scale damage analysis in composite and porous materials. *International Journal of Solids and Structures* 2001; **38**(14):2335–2385.
18. Raghavan P, Ghosh S. Concurrent multi-scale analysis of elastic composites by a multi-level computational model. *Computer Methods in Applied Mechanics and Engineering* 2004; **5**(2):151–170.
19. Fish J, Shek K. Multiscale analysis of composite materials and structures. *Composites Science and Technology* 2000; **60**:2547–2556.
20. Fish J, Yu Q, Shek K. Computational damage mechanics for composite materials based on mathematical homogenization. *International Journal for Numerical Methods in Engineering* 1999; **45**:1657–1679.
21. Hao S, Liu WK, Moran B, Vernerey F, Olson GB. Multi-scale constitutive model and computational framework for the design of ultra-high strength, high toughness steels. *Computer Methods in Applied Mechanics and Engineering* 2004; **193**(17–20):1865–1908.
22. Hao S, Moran B, Liu WK, Olson GB. A Hierarchical multi-physics model for design of high toughness steels. *Journal of Computer-Aided Materials Design* 2003; **10**:99–142.
23. Oden JT, Zohdi TI. Analysis and adaptive modeling of highly heterogeneous elastic structures. *Computer Methods in Applied Mechanics and Engineering* 1997; **148**:367–391.
24. Vemaganti K, Oden JT. Estimation of local modeling error and goal-oriented adaptive modeling of heterogeneous materials, Part II: A computational environment for adaptive modeling of heterogeneous elastic solids. *Computer Methods in Applied Mechanics and Engineering* 2001; **190**:6089–6124.
25. Terada K, Kikuchi N. Simulation of the multi-scale convergence in computational homogenization approaches. *International Journal of Solids and Structures* 2000; **37**:2285–2311.
26. Zohdi TI, Wriggers P. A domain decomposition method for bodies with heterogeneous microstructure based on material regularization. *International Journal of Solids and Structures* 1999; **36**:2507–2525.
27. Chung PW, Tamma KK. Woven fabric composites: developments in engineering bounds, homogenization and applications. *International Journal for Numerical Methods in Engineering* 1999; **45**:1757–1790.
28. Raghavan P, Li S, Ghosh S. Two scale response and damage modeling of composite materials. *Finite Elements in Analysis and Design* 2004; **40**(12):1619–1640.
29. Xia Z, Curtin WA, Peters PWM. Multiscale modeling of failure in metal matrix composites. *Acta Materialia* 2001; **49**:273–287.
30. Gokhale AM, Yang S. Application of image processing for simulation of mechanical response of multi-length scale microstructures of engineering alloys. *Metallurgical and Materials Transactions A* 1999; **30**:2369–2381.
31. Tewari A, Gokhale AM, Spowart JE, Miracle DB. Quantitative characterization of spatial clustering in three-dimensional microstructures using two-point correlation functions. *Acta Materialia* 2004; **52**:307–319.
32. Yeong CLY, Torquato S. Reconstructing random media. *Physical Review E* 1998; **57**:495–505.
33. Rintoul MD, Torquato S. Reconstruction of structure of dispersions. *Journal of Colloid and Interface Science* 1996; **186**:467–476.
34. Manwart C, Torquato S, Hilfer R. Stochastic reconstruction of sandstones. *Physical Review E* 2000; **62**:893–899.
35. Yang N, Boselli J, Sinclair I. Simulation and quantitative assessment of homogeneous and inhomogeneous particle distributions in particulate metal matrix composites. *Journal of Microscopy* 2000; **201**:189–200.
36. Cooper DW. Random sequential packing simulation in three dimensions for spheres. *Physical Review A* 1998; **38**:522–524.
37. Everett RK, Chu JH. Modeling of non-uniform composite microstructures. *Journal of Composite Materials* 1992; **27**:1128–1144.
38. Freeman, Pasztor EC, Carmichael OT. Learning low-level vision. *International Journal of Computer Vision* 2000; **40**:24–47.

DOI: 10.1002/nme

39. Robert RK. Cubic convolution interpolation for digital image processing. *IEEE Transactions on Acoustics*, *Speech and Signal Processing* 1981; **ASSP-29**:1153–1160.
40. Unser M, Aldroubi A, Eden M. Fast B-spline transforms for continuous image representation and interpolation. *IEEE Transactions on Pattern Analysis and Machine Intelligence* 1991; **13**:277–285.
41. Jensen K, Anastassiou D. Subpixel edge localization and the interpolation of still images. *IEEE Transactions on Image Processing* 1995; **4**:285–295.
42. Prasad L, Iyengar SS. *Wavelet Analysis with Applications to Image Processing*. CRC Press: Boca Raton, FL, 1997.
43. Torquato S. *Random Heterogeneous Materials*: *Microstructure and Macroscopic Properties*. Springer: New York, 2002.
44. Chui CK. *An Introduction to Wavelets*. Academic Press: New York, 1992.
45. Qian S, Weiss J. Wavelets and the numerical solution of boundary value problems. *Applied Mathematics Letters* 1993; **6**(1):47–52.
46. Everson R, Sirovich L, Sreenivasan KR. Wavelet analysis of the turbulent jet. *Physics Letters A* 1990; **145**:314–322.
47. Lewalle J. Wavelet analysis of experimental data: some methods and the underlying physics. *AIAA 94-2281*, *25th AIM Fluid Dynamics Colorado Springs*, 1994.
48. Sahoo PK, Soltani S, Wong AKC. A survey of thresholding techniques. *Computer Vision Graphics Image Process* 1988; **41**:233–260.
49. Luthon F, Lievin M, Faux F. On the use of entropy power for threshold selection. *Signal Processing* 2004; **84**:1789–1804.
50. Russ JC. *The Image Processing Handbook*. CRC/IEEE Press: Boca Raton/New York, 1999.
51. Caceres CH, Griffiths JR, Reiner P. The influence of microstructure on the Bauschinger effect in as Al–Si–Mg casting alloy. *Acta Materialia* 1996; **44**:15–23.
52. Caceres CH, Davidson CJ, Griffiths JR, Wang QG. The effect of Mg on the microstructure and mechanical behavior of Al–Si–Mg Casting alloys. *Metallurgical and Materials Transactions A* 1999; **30**:2611–2618.
53. Seul M, O'Gorman L, Sammon MJ. *Practical Algorithms for Image Analysis*. Cambridge University Press: Cambridge, MA, 2000.
54. Spitzig WA, Kelly JF, Richmond O. Quantitative characterization of second-phase populations. *Metallography* 1985; **18**:235–261.
55. Li M, Ghosh S, Richmond O, Weiland H, Rouns TN. Three dimensional characterization and modeling of particle reinforced metal matrix composites part II: Damage characterization. *Materials Science and Engineering A* 1999; **266**:221–240.
56. Ghosh S, Nowak Z, Lee K. Tessellation-based computational methods for the characterization and analysis of heterogeneous microstructures. *Composites Science and Technology* 1997; **57**:1187–1210.
57. Ghosh S, Nowak Z, Lee K. Quantitative characterization and modeling of composite microstructures by voronoi cells. *Acta Materialia* 1997; **45**:2215–2234.
58. Yotte S, Riss J, Breysse D, Ghosh S. PMMC cluster analysis. *Computer Modeling in Engineering and Sciences* 2004; **5**:171–187.
59. Karnezis PA, Durrant G, Cantor B. Characterization of reinforced distribution in cast Al-Alloy/SiC composites. *Materials Characterization* 1998; **40**:97–109.
60. Anson JP, Gruzleski JE. The quantitative discrimination between shrinkage and gas microporosity in cast aluminum alloys using spatial data analysis. *Materials Characterization* 1999; **43**:319–335.
61. Serra J. *Image Analysis and Mathematical Morphology*. Academic Press: New York, 1982.
62. Swaminathan S, Ghosh S, Pagano NJ. Statistically equivalent representative volume elements for unidirectional composite microstructures: Part I—without damage. *Journal of Composite Materials* 2006; **40**:583–604.
63. Spowart JE, Mayurama B, Miracle DB. Multiscale characterization of spatially heterogeneous systems: implications for discontinuously reinforced metal-matrix composite microstructures. *Materials Science and Engineering A* 2001; **307**:51–66.

DOI: 10.1002/nme